Setdb1 safeguards genome integrity in muscle stem cells to allow for regenerative myogenesis and inflammation

Pauline Garcia[a], William Jarassier[a], Caroline Brun[a], Lorenzo Giordani[b], Cécile Peccate[b], Fany Agostini[a], Wai Hing Kung[c], Tom H Cheung[c] and Fabien Le Grand[a]

[a] Université Claude Bernard Lyon 1, CNRS UMR 5261, INSERM U1315, Institut NeuroMyoGène, Pathophysiology and Genetics of Neuron and Muscle (PGNM) Unit, 69008 Lyon, France.
[b] Sorbonne Université, Inserm UMRS 974, Institut de Myologie, Myology Research Center Unit, F-75013 Paris, France
[c] Division of Life Science, Center for Stem Cell Research, HKUST-Nan Fung Life Sciences Joint Laboratory, State Key Laboratory of Molecular Neuroscience, Molecular Neuroscience Center, The Hong Kong University of Science and Technology, Hong Kong, China.

Correspondence should be addressed to fabien.le-grand@cnrs.fr

Abstract

Modulations in chromatin structure orchestrate gene expression and direct stem cell fate. More specifically, the Histone 3 Lysine 9 Methyltransferase SETDB1 controls transcriptional repression to regulate pluripotency and self-renewal. While SETDB1 functions have been extensively studied in embryonic stem cells and in cancer cells, less is known on the role of SETDB1 in adult stem cells *in vivo*. Here, we show that SETDB1 expression by adult muscle stem cells (MuSCs) is absolutely required for muscle tissue regeneration following acute injury. We find that SETDB1 represses the expression of the endogenous retroviruses (ERVs) family of transposable elements in MuSCs. ERV re-expression in *Setdb1-null* MuSCs prevents their amplification following exit from quiescence and promotes cell death. Multi-omics profiling further shows that the absence of SETDB1 in MuSCs leads to the activation of the DNA-sensing cGAS-STING pathway, entailing activation of the Interferon pathway and increased cytokine expression. *In vivo*, the cytokine storm triggered by MuSCs devoid of *Setdb1* provokes aberrant infiltration of inflammatory cells including the appearance of a pathological macrophage lineage. The ensuing histiocytosis results in necrosis of the newly formed muscle fibers and completely abolishes skeletal muscle tissue repair. In contrast, disruption of *Setdb1* gene in another muscle-resident cell type, the fibro-adipogenic progenitors (FAPs), does not lead to any phenotype. In conclusion, the control of genome stability by SETDB1 in an adult somatic stem cell is necessary for both its regenerative potential and its adequate communication with the inflammatory cells regulating tissue repair.

Keywords: Histone Methyltransferase, Regeneration, Muscle Stem cells, Endogenous Retroviruses, Cytokine Storm

Introduction

The timing of gene expression in stem cells is crucial for proper lineage commitment, cell fate determination, and regeneration.[1] Chromatin structure regulates gene expression and stem cell fate choices, and its deregulation is linked to developmental defects, diseases, and aging.[2] Lysine methyltransferases (KMT) and demethylases (KDM) are critical regulators of chromatin. Histone 3 methylation at lysine position 9 (H3K9) is necessary for the assembly of constitutive and facultative heterochromatin. SUV39 family KMTs, including SUV39H1/2, G9A, GLP, and SETDB1/2, primarily methylate H3K9. Although these KMTs can substitute for each other in some cases, their functions are not interchangeable. SETDB1 (SET domain bifurcated histone lysine methyltransferase 1, also called ESET or KMT1E) is responsible for H3K9 di- and tri-methylation involved in gene repression in euchromatin and facultative heterochromatin.[3] SETDB1 is required for transcriptional repression, pluripotency, and self-renewal of mouse embryonic stem cells (mESCs).[4]

Gain-of-function mutations of SETDB1 are associated with various types of cancer, promoting cell cycle, proliferation, migration, and invasion of cancer cells.[5,6] While the functions of SETDB1 have been extensively studied in embryonic stem and cancer cells, little is known about its role in adult stem cells *in vivo*, and no studies have investigated its impact on adult tissue regeneration following injury.

Adult skeletal muscle consists of multinucleated innervated myofibers that ensure muscle functions and contractility. Myofibers carry a population of quiescent muscle stem cells (MuSCs) in a niche between their plasma membrane and the surrounding basal lamina.[7] MuSCs have the ability to repair and form *de novo* myofibers to regenerate damaged muscle tissue. Following injury of their host myofibers, MuSCs activate from quiescence, give rise to transient amplifying muscle progenitor cells (also called myoblasts) that will differentiate and fuse into myotubes that subsequently mature into myofibers.[8] Understanding the molecular and cellular mechanisms that regulate MuSC activation, proliferation, and differentiation is crucial for developing therapies.

Previous research found that SETDB1 is highly expressed in activated MuSCs, primarily nuclear, but relocates to the cytoplasm upon myoblast differentiation in a canonical WNT signaling-dependent manner. This differential localization of SETDB1 corresponds to a change in the gene expression program required for myoblast terminal differentiation.[9] However, the role of SETDB1 in proliferative MuSCs during muscle regeneration is unknown. To investigate this, we generated a conditional mouse model that allows the targeted deletion of *Setdb1* in MuSCs. *In vitro*, *ex vivo*, and *in vivo* analyses were performed to gain insights into the functions of SETDB1 in MuSCs, specifically during muscle regeneration.

Results

SETDB1 is required for muscle regeneration

To study the role of *Setdb1*-mediated gene silencing in MuSCs during skeletal muscle regeneration, we crossed mice harboring a floxed *Setdb1* allele[10] with mice expressing CreERT2 from the Pax7 locus as a bicistronic transcript[11] (Figure S1A). To induce recombination at the *Setdb1* loci in MuSCs, we injected 10-week-old *Pax7*$^{CreERT2/+}$:*Setdb1*$^{lox/lox}$ mice (named *Setdb1*-cKO mice) with tamoxifen (*Setdb1*$^{MuSC\text{-}KO}$) diluted in corn oil. For controls, we injected mice of the same genotype with corn oil only (*Control*). Genotyping PCR of MuSCs isolated from TAM-induced mice showed an 85% efficiency in *Setdb1* allele deletion as compared to oil-treated mice (Figure S1B).

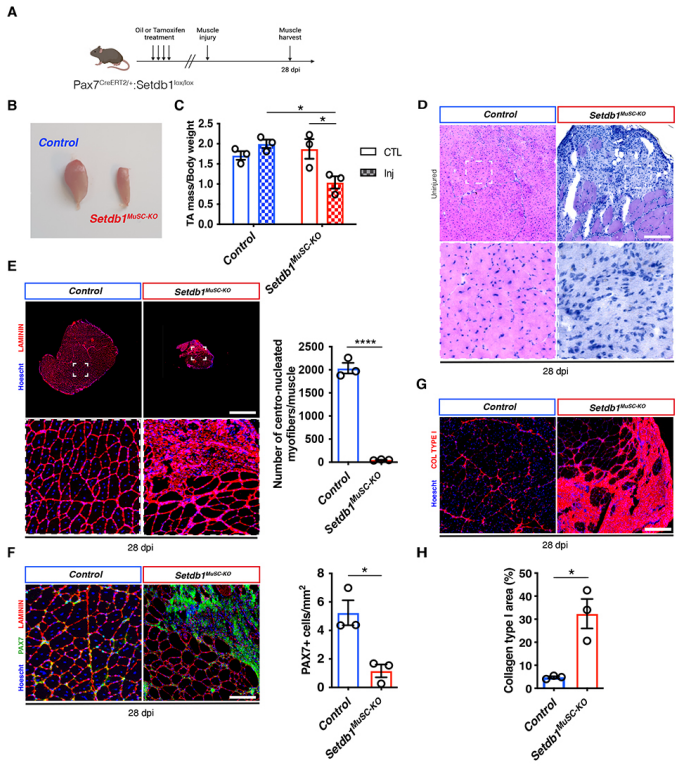

Figure 1. *(A) Experimental scheme; Pax7*$^{CRE\text{-}ERT2}$*; Setdb1*$^{fl/fl}$ *mice intraperitoneally injected with either Oil or Tamoxifen and cardiotoxin (CTX) is performed on TA (Tibialis Anterior) muscle after 28 days post injury. (B) Representative photographs representing TA muscle after 28 days post injury in both conditions. (C) Normalized TA weight on mice body weight represented in Control and Setdb1*$^{MuSC\text{-}KO}$ *conditions in uninjured and injured TA (n=3 mice). (D) Hematoxylin and eosin stain of TA muscle cross sections at 28 days post injury (CTX) (n=3 mice). (E) Immunostaining for LAMININ on TA cryosections 28 days after injury. Quantification of the number of centro-nucleated myofibers on TA cryosections 28 days after injury (n=3 mice). (F) Quantification of PAX7+ cells on TA cryosections for the Control and Setdb1*$^{MuSC\text{-}KO}$ *conditions (n=3 mice). (G) COLLAGEN I immunostaining on TA cryosections 28 days after injury (n=3 mice). (H) Quantification of the COLLAGEN I area in Control and Setdb1*$^{MuSC\text{-}KO}$ *conditions. Data are represented as mean ± SEM;* $^{*}p < 0.05$, $^{****}p < 0.0001$, *t test. Scale bars, (E) 200 µm, (F) 100 µm, (G) 150 µm.*

MuSCs are mostly quiescent, as only a minute proportion (2 to 4%) can be seen cycling in adult muscles.[12] As such, we examined if conditional *Setdb1* gene disruption could induce MuSCs to leave their quiescent state. Three months after tamoxifen treatment, control and *Setdb1*$^{MuSC\text{-}KO}$ mice exhibited similar numbers of sublaminar PAX7+ MuSCs (Figure S1D). Furthermore, we did not observe any alterations of anatomy, histology and myofiber size in *Setdb1*$^{MuSC\text{-}KO}$ Tibialis Anterior (TA) muscles (Figure S1C, S1E, S1F). Together, our observations indicate that *Setdb1* gene disruption does not perturb the quiescent MuSC pool and therefore, SETDB1 is not required to control MuSC quiescence.

To determine if *Setdb1*$^{MuSC\text{-}KO}$ can support injury-induced adult regenerative myogenesis, we injured TA muscles using cardiotoxin[13] and sampled the tissues 28 days post-injury (d.p.i.) (Figure 1A). While the control muscles appeared well regenerated, *Setdb1*$^{MuSC\text{-}KO}$ muscles were severely reduced in size (Figure 1B), exhibiting more than a 50% decreased mass compared to either the contralateral (CTL) or the regenerated control TA muscle (Figure 1C).

Hematoxylin and eosin (H&E) staining of tissue cross-sections showed that deletion of *Setdb1* in MuSCs completely abrogated the tissue regeneration process (Figure 1D). As such, injured *Setdb1*$^{MuSC\text{-}KO}$ muscles did not contain any new myofibers as compared to injured controls that were mostly composed of regenerated myofibers with centrally-located nuclei (Figure 1E). This impairment of regenerative process was accompanied by a 5-fold reduction in the numbers of PAX7^{+} MuSCs (Figure 1F). Investigation of the nature of the residual tissue composing the injured *Setdb1*$^{MuSC\text{-}KO}$ muscles revealed that myofibers were replaced by a scar tissue composed of a Collagen Type I matrix (Figure 1G-H). Thus, *Setdb1* expression in MuSCs is absolutely required for injury-induced adult myogenesis.

MuSC proliferation and viability rely on SETDB1

Our first *in vivo* regeneration analysis highlights that loss of *Setdb1* in MuSCs completely block muscle tissue repair. To understand the consequences of *Setdb1* gene disruption at the MuSC scale, we performed *ex vivo* experiments using isolated and cultured single *Extensor Digitalis Longus* (EDL) myofibers (Figure 2A, Figure S2A) and 5-ethynyl-2'-deoxyuridine (EdU) incorporation assay. After 24 hour-culture, the numbers of MuSCs *per* fiber was similar between *Control* and conditional-null samples (Figure S2B). However, *Setdb1*$^{MuSC\text{-}KO}$ myofibers had lower amounts of EdU^{+} MuSCs compared to controls, indicating MuSC delayed entry into S-phase upon *Setdb1* deletion (Figure S2C). Moreover, 72h-cultured *Setdb1*$^{MuSC\text{-}KO}$ myofibers exhibited a 3-fold decrease in the numbers of MuSCs *per* fiber, and only 6% of *Setdb1*$^{MuSC\text{-}KO}$ MuSCs incorporated EdU, compared to 17% in controls (Figure 2C-D, Figure S2D). Altogether, these results demonstrate that loss of *Setdb1* triggers proliferation defect. Of note, the percentage of MYOG^{+} differentiating cells on single myofibers at 72h was not significantly different between *Setdb1*$^{MuSC\text{-}KO}$ and *Control* samples, indicating the amplification defect was not due to premature differentiation (Figure S2E). These data suggest that SETDB1 plays a major role for MuSC amplification following exit from quiescence.

To confirm these results, MuSCs were MACS-sorted from *Control* and *Setdb1*$^{MuSC\text{-}KO}$ muscles and grown *in vitro* (Figure 2B). While we observed no difference between genotypes at day 3 post-extraction, *Setdb1*$^{MuSC\text{-}KO}$ MuSCs presented a striking deficit in colony formation after 7 days *in vitro* (Figure 2E, Figure S2F). The almost complete absence of amplification potential of *Setdb1*$^{MuSC\text{-}KO}$ MuSCs *in vitro* thus precluded more detailed analysis of their phenotype. To overcome this pitfall, we extracted MuSCs from un-treated *Setdb1*-cKO mice and cultured them in vitro. Following *in vitro* amplification, primary cells were then treated with either vehicle (EtOH) or 4-hydroxitamoxifen (4-OHT) for 3 days *in vitro* to induce *Setdb1* gene recombination (Figure 2F).

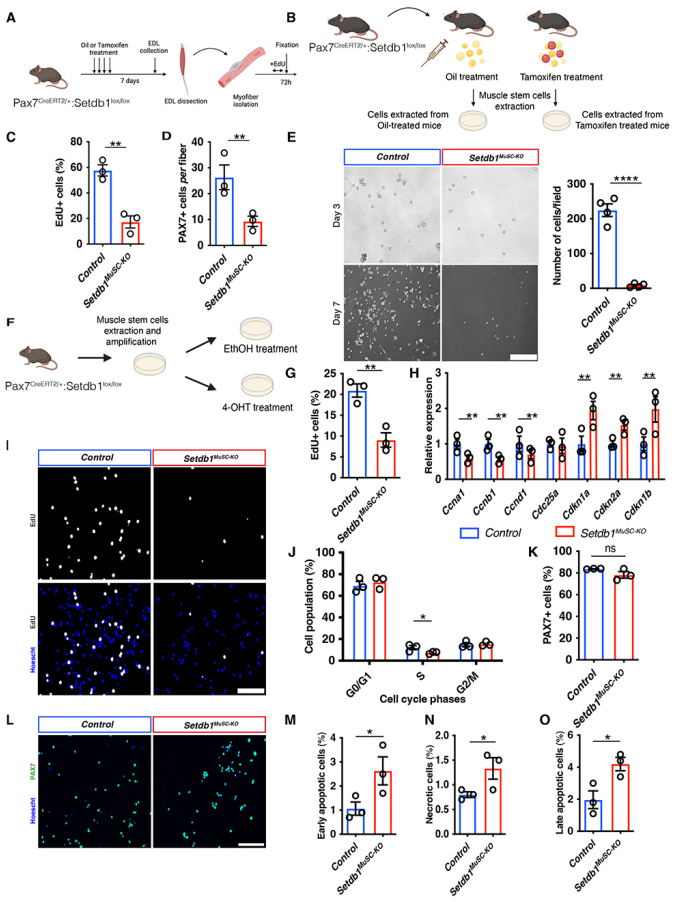

Figure 2. *(A) Experimental se up of isolated myofibers ex vivo during 72 hours after oil and Tamoxifen treatment in the Pax7$^{CRE-ERT2}$; Setdb1$^{fl/fl}$ mice (B) Experimental scheme of the set up used to extract myoblasts in culture in vitro after oil and Tamoxifen treatment of the Pax7$^{CRE-ERT2}$; Setdb1$^{fl/fl}$ mice model. (C) Quantification of EdU+ cells on isolated myofiber after 72h in culture ex vivo in Control and Setdb1$^{MuSC-KO}$ cells (n=3). (D) Quantification of PAX7+ cells on isolated myofiber after 72h in culture ex vivo in Control and Setdb1$^{MuSC-KO}$ cells (n=3). (E) Photographs representing the extracted myoblasts after 3 days and 7 days in vitro from the Control and Setdb1$^{MuSC-KO}$ mice. Quantification of the cell number in the Control and Setdb1$^{MuSC-KO}$ cells in vitro after 7 days (n=4). (F) Experimental scheme used to analyze the myoblasts in culture in vitro in both conditions Control (treated with Ethanol (EtOH)) and Setdb1$^{MuSC-KO}$ (treated with 4-Hydroxitamoxifen (4-OHT)) condition. (G) Quantification of the number of EdU+ cells Control and Setdb1$^{MuSC-KO}$ after EtOH and 4-OHT treatment (n=3). (H) Relative expression of genes that positively (Ccna1, Ccnb1, Ccnd1 and Cdc25a) or negatively (Cdkn1a, Cdkn2a and Cdkn1b) regulates cell cycle after 5 days of EtOH or 4-OHT treatment (n=3). (I) EdU immunostaining after 5 days of EtOH and 4-OHT treatment and quantification of EdU+ cells (n=3).*
(J) Flow cytometry analysis of cell cycle phases obtained following Propidium iodide staining (n=3). (K) Quantification of PAX7+ cells after 5 days of EtOH and 4-OHT treatment in the Control and Setdb1$^{MuSC-KO}$ cells (n=3). (L) Immunostaining of PAX7+ cells after 5 days of EtOH and 4-OHT treatment (n=3). (M) Flow cytometry plots using Propidium Iodide staining and Yo-Pro and quantification of the early apoptotic cells in the Control and Setdb1$^{MuSC-KO}$ cells (n=3). (N) Quantification of the late apoptotic cells in the Control and Setdb1$^{MuSC-KO}$ cells (n=3). (O) Quantification of the necrotic cells in the Control and Setdb1$^{MuSC-KO}$ cells (n=3). Data are represented as mean ± SEM; n.s not significant, $^{*}p < 0.05$, $^{**}p < 0.01$, $^{****}p < 0.0001$, t test. Scale bars, (E) 150 µm (I) 100 µm (L) 100 µm.

4-OHT treatment reduced the proliferation of primary cells *in vitro*, as shown by decreased EdU incorporation (Figure 2G-I) and decreased proportion of phospho-Histone H3-positive cells (Figure S2G). Accordingly, quantitative RT-PCR revealed that the gene expression of several cyclins (*Ccna1*, *Ccnb1*, *Ccnd1* and *Cdc25a*) was significantly reduced in *Setdb1$^{MuSC-KO}$* cells while the expression of cyclin-dependent-kinase inhibitors (*Cdkn1a*, *Cdkn2a* and *Cdkn1b*) was increased (Figure 2H). Cell cycle analysis by flow cytometry using Propidium Iodide (PI) delineated a specific decrease in the fraction of cells in S-phase in *Setdb1$^{MuSC-KO}$* cells compared to *Control* cells (Figure 2J). Importantly, immunostaining for the MuSC marker PAX7 as well as gene expression analysis for *Pax7*, *Myod1* and *Myog* did not show any significant difference between vehicle-treated and 4-OHT-treated cells (Figure 2K-L, Figure S2H), indicating that the proliferation defect induced by *Setdb1* gene disruption is not related to a loss of myogenic identity. We next stained cells with PI and YO-PRO®-1 to evaluate the percentage of early and late apoptotic cells, as well as the number of necrotic cells, by flow cytometry. Interestingly, the *Setdb1$^{MuSC-KO}$* cells exhibited an increase of the three conditions, demonstrating that the loss of *Setdb1* leads to cell death (Figure 2M-O).

To analyze if *Setdb1* gene disruption could affect the myogenic differentiation process, we treated proliferating cells with either EtOH or 4-OHT for 3 days and then, shifted the cultures into differentiation medium for another 3 days. Of note, the starting number of cells was higher in the 4-OHT condition, to compensate for the reduced growth rate. Immunostaining for Myosin Heavy Chains (MyHC), accompanied by the quantification of differentiated nuclei and fused nuclei (Figure S2J-2K) and the number of myonuclei *per* myotubes (Figure S2L) did not reveal any difference between *Control* and *Setdb1$^{MuSC-KO}$* conditions. We concluded that the loss of *Setdb1* did not impact myogenic differentiation. Taken together, our *ex vivo* and *in vitro* data highlight that SETDB1 is crucial for MuSC proliferation and viability.

Loss of Setdb1 expression in MuSCs delays myofiber formation

To evaluate if the absence of regenerative potential in *Setdb1$^{MuSC-KO}$* mice is only attributable to a decreased amplification of MuSCs following their activation from quiescence, we performed injury experiments and sampled the regenerating tissues at early time-points (Figure 3A). Intriguingly, we did not observe a difference in the mass of *Setdb1$^{MuSC-KO}$* muscles compared to *Control* muscles at 4 d.p.i. (Figure 3B). At 7 d.p.i. the weight of the injured *Setdb1$^{MuSC-KO}$* muscles weights was closer to their contralateral than the *Control* ones (Figure 3C). However, examination of regenerating tissue cross-sections revealed perturbations in the regeneration process in *Setdb1$^{MuSC-KO}$* muscles. Indeed, at 4 d.p.i., we observed a drastic loss of MuSCs within the *Setdb1$^{MuSC-KO}$* muscles as compared to the *Control* (Figure 3D). In contrast, measurement of the cross-sectional area of newly-formed myofibers did not show any difference between the different conditions. (Figure 3F-G). However, the regenerating *Setdb1$^{MuSC-KO}$* muscles were disorganized compared to *Control* muscles, showing a 15% increase in the intermembrane space between the myofibers (Figure S3A-B). At 7 d.p.i., tissue disorganization augmented in *Setdb1$^{MuSC-KO}$* muscles, with myofibers displaying aberrant shapes (Figure 3E, Figure S3D). Indeed, cross-sectional area measurement showed severe atrophy of regenerated *Setdb1$^{MuSC-KO}$* myofibers (Figure 3H, Figure 3I). Consistent with our observations at 4 d.p.i., more than 70% of MuSCs were lost in *Setdb1$^{MuSC-KO}$* muscles compared to *Controls* (Figure 3E). From these results, we conclude that muscle regeneration is strongly affected in the absence of *Setdb1* expression by MuSCs, although new myofibers can still be formed.

To evaluate the maturation of newly-formed myofibers, we performed immunostaining against embryonic forms of Myosin Heavy Chains (eMyHC). This Myosin isoform is specifically expressed by newly formed myofibers during muscle regeneration at early timepoints

and is absent from well-regenerated myofibers. At 4 d.p.i., a strong reduction of the number of eMyHC+ myofibers was found in the *Setdb1*$^{MuSC\text{-}KO}$ muscles compared to control muscles, indicating a delay in myogenesis (Figure 3J). Surprisingly, at 7 d.p.i., almost all of the regenerating myofibers were positive for eMyHC+ in *Setdb1*$^{MuSC\text{-}KO}$ muscles, while it had become hardly detectable in *Control* muscles (Figure 3K). The relative expression of *Pax7*, *Myh4* (adult isoform), *Myh8* (peri-natal isoform) observed at 7 d.p.i confirmed these results (Figure S3E). Taken together, these data suggest that myofibers regenerated from *Setdb1*-null MuSCs do not develop properly.

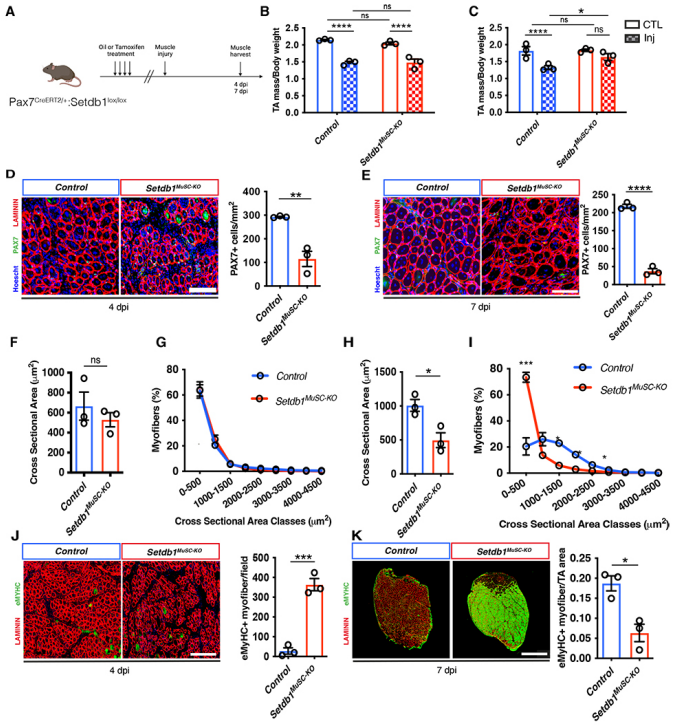

Figure 3. *(A) Experimental set up; Pax7*$^{CRE\text{-}ERT2}$*; Setdb1*$^{fl/fl}$ *mice intraperitoneally injected with either Oil or Tamoxifen. Cardiotoxin-induced injury (CTX) was performed in the TA (Tibialis Anterior) muscles and analyzed 4- and 7-days post-injury. (B) Normalized TA weight on mice body weight represented in Control and Setdb1*$^{MuSC\text{-}KO}$ *muscles in uninjured and injured TA after 4 days post injury (n=3 mice). (C) Normalized TA weight on mice body weight represented in Control and Setdb1*$^{MuSC\text{-}KO}$ *muscles in uninjured and injured TA after 7 days post injury (n=3 mice). (D) LAMININ and PAX7 immunostaining in Control and Setdb1*$^{MuSC\text{-}KO}$ *muscles after 4 days of the CTX injury and quantification of the PAX7+ cells in both conditions (n=3 mice). (E) LAMININ and PAX7 immunostaining in Control and Setdb1*$^{MuSC\text{-}KO}$ *muscles after 7 days of the CTX injury and quantification of the PAX7+ cells in both conditions (n=3 mice). (F) Cross sectional area of CTX-injured TA muscles of Control and Setdb1*$^{MuSC\text{-}KO}$ *muscles after 4 days post injury (n=3 mice). (G) Distribution of cross-sectional area of CTX-injured TA muscles, as determined in F (n=3 mice). (H) Cross sectional area of CTX-injured TA muscles of Control and Setdb1*$^{MuSC\text{-}KO}$ *muscles after 7 days post injury (n=3 mice). (I) Distribution of cross-sectional area of CTX-injured TA muscles, as determined in F (n=3 mice). (J) eMYHC and LAMININ immunostaining in Control and Setdb1*$^{MuSC\text{-}KO}$ *muscles at 4 days after injury and quantification of the number of eMYHC+ myofibers per cryosections (n=3 mice). (K) eMYHC and LAMININ immunostaining in Control and Setdb1*$^{MuSC\text{-}KO}$ *muscles at 7 days after injury and quantification of the number of eMYHC+ myofibers per field (n=3 mice). Data are represented as mean ± SEM; n.s not significant,* $^{*}p < 0.05$, $^{**}p < 0.01$, $^{***}p < 0.001$, $^{****}p < 0.0001$, *t test. Scale bars, (D) 100 µm (E) 20 µm (J) 50 µm (K) 400 µm*

Muscle regeneration requires a crosstalk between the different cell types inhabiting the tissue. As such, a delay of a defect in myogenesis is often associated with a compensatory growth of other cell types. Accordingly, we quantified increased amounts of PDGFRα+ fibro-adipogenic progenitors (FAPs) in regenerating *Setdb1*$^{MuSC\text{-}KO}$ muscle compared to control muscles (Figure S3C).

Taken together, these results show that MuSC-specific *Setdb1* gene disruption leads to impaired muscle regeneration accompanied by fibrosis. However, *de novo* myofiber formation is still present, albeit severely perturbed.

SETDB1 restricts chromatin accessibility at TE sites in MuSCs to prevent cGAS-STING activation

To understand the functional basis of the observed phenotype, we performed RNA-sequencing (RNA-seq) on MuSCs isolated by fluorescence-activated cell sorting (FACS) from 60 hours-regenerating muscles (Figure S4A). Of note, RNA-seq validated *Setdb1* gene recombination efficiency (Figure S4B). We observed a global impact on MuSC gene expression in absence of *Setdb1* (Figure 4B, Figure S4C). Correlating with the phenotype observed of MuSCs *in vitro* and *in vivo*, gene set enrichment analysis revealed an enrichment for signaling related to 'Apoptosis' and 'p53 pathways' in *Setdb1*$^{MuSC\text{-}KO}$ cells (Figure 4A; Table 1). Likewise, *Setdb1*$^{MuSC\text{-}KO}$ cells showed reduced expression of genes associated with cell cycle progression (Figures S4D). *Setdb1*$^{MuSC\text{-}KO}$ cells also exhibited enrichment for pathways related to 'Immune response and Inflammation', 'DNA damage' and 'Xenobiotic stress' (Figure 4A), the latter being associated with a massive upregulation of glutathione S-transferase genes (for instance, *Gsta4*) in *Setdb1*$^{MuSC\text{-}KO}$ (Figure 4B). GSTs have a key role in the biotransformation of substances that are not naturally expected to be present within the organism of which can be the products of transposable elements (TE)[1415]. Since SETDB1 is critical for TE silencing in mESCs[10,16], we analyzed the expression of repetitive elements. Remarkably, *Setdb1*$^{MuSC\text{-}KO}$ MuSCs displayed re-expression of TEs of the Long Terminal Repeat family (LTRs) (Figure S4E). Among these LTRs, we found transcripts of the endogenous retrovirus (ERVs) class, notably of the ERVK and ERV1 subfamilies (Figure S4F). The most statistically significant TEs re-expressed by *Setdb1*$^{MuSC\text{-}KO}$ MuSCs were ERVKs (Figure 4C) and included elements already described as SETDB1 targets, such as *RTLR6B* or *MMERVK10C*.[17,18]

As SETDB1 controls DNA folding and subsequent gene repression, we thus investigated chromatin compaction at ERVs loci in Control and *Setdb1*$^{MuSC\text{-}KO}$. *Setdb1*$^{MuSC\text{-}KO}$. To this end, we performed Assay for Transposase-Accessible Chromatin with sequencing (ATAC-seq) on cultured MuSCs treated with either EtOH or 4-OHT *in vitro* (Figure S4G, S4I). Of note, we chose not to perform ATAC-seq on FACS-sorted cells, since a high prevalence of dying cells is incompatible with ATAC-seq. Principal component analysis (PCA) revealed that chromatin accessibility landscape of *Setdb1*$^{MuSC\text{-}KO}$ MuSCs *in vitro* was significantly different from *Control* MuSCs (Figure S4H). Peak calling and differential analysis of accessible sites demonstrated a global increase in Chromatin accessibility in *Setdb1*$^{MuSC\text{-}KO}$ MuSCs compared to *Control* cells (Figure 4F). Evaluating the signals specific to each condition showed *Setdb1*$^{MuSC\text{-}KO}$ cells displayed 17,387 specific peaks on the 97,598 total peaks, suggesting that the loss of *Setdb1* leads to chromatin opening at specific loci (Figure 4D; Table 2). This release of chromatin compaction in *Setdb1*$^{MuSC\text{-}KO}$ cells was accompanied by increased DNA damage and enlarged nuclei diameter (Figure 4E). Interestingly, visualization of enriched pathways from differentially accessible chromatin in *Setdb1*$^{MuSC\text{-}KO}$ cells compared to *Control* cells

highlighted 'Regulation of Chemokine' as the most enriched signaling (Figure S4J).

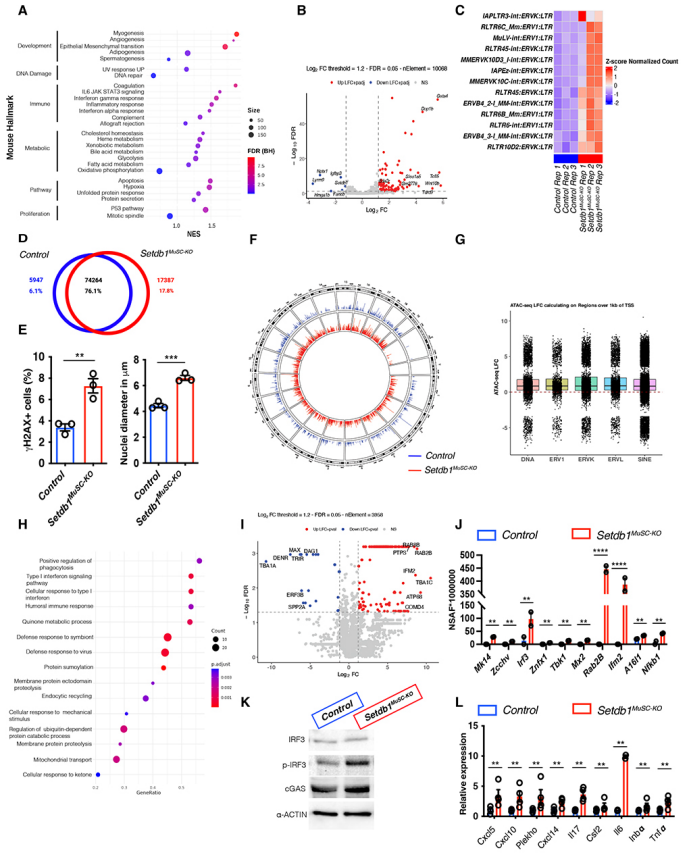

Figure 4. *(A) Results of GSEA showing enriched gene sets from Mouse Hallmark on upregulated genes in Setdb1$^{MuSC-KO}$ muscles (n=3). Gene sets are grouped by process. Dot in red indicate a high significant enrichment (adjusted by FDR), dot in blue indicate a low significant enrichment. The size shows the number of gene dysregulated in each gene set and results are ordering in high to low level of Normalized Enrichment Score (NES). (B) Volcano plot over Setdb1$^{MuSC-KO}$ muscles RNA-seq data (n=3). Dot in colors indicate significant dysregulated genes (FDR<0.05): in red, up-dysregulated (Log2 Fold-Change (LFC)>=1), in blue down-dysregulated (LFC<=-1). Dot in grey indicate no significant dysregulated genes or low value of LFC (abs(LFC)<1). (C) Heatmap of RNA-Seq normalized expression z-scores computed for upregulated ERVs found in Setdb1$^{MuSC-KO}$ sorted MuSCs (n=3 mice). (D) Venn diagram showing overlapping ATAC-seq binding regions shared or not between Control and Setdb1$^{MuSC-KO}$ cells in vitro. (E) Quantification of the γH2AX+ cells in Control and Setdb1$^{MuSC-KO}$ cells in vitro and measurement of the nuclei diameter in Control and Setdb1$^{MuSC-KO}$ cells in vitro (n=3). (F) Genomic distribution of high ATAC-seq peaks (log10 (peak score) > 1.2) on mouse genome for Control and Setdb1$^{MuSC-KO}$ cells in vitro (n=2). (G) Results of differential open-region analysis between Control and Setdb1$^{MuSC-KO}$ (n=2) for open-region containing at least one transposable element for five different group (DNA, ERV1, ERVK and ERVL, SINE). (H) Results of GSEA showing enriched gene sets from Gene Ontology Biological Process on dysregulated protein in Setdb1$^{MuSC-KO}$ cells (n=2). Selected enriched terms are presented according to the fold enrichment. Dot in red indicate a high significant enrichment (adjusted by FDR), dot in blue indicate a low significant enrichment. The size shows the number of gene dysregulated in each gene set and results are ordering in high to low protein ratio observed/expected. (I) Volcano plot over Setdb1$^{MuSC-KO}$ cells proteomic data (n=2). Significantly dysregulated genes are highlighted in red (FDR < 0.05). Dot in colors indicate significant dysregulated genes (FDR<0.05): in red, up-regulated (Log2 Fold-Change (LFC)>=1.2), in blue down-regulated (LFC<=-1). Dot in grey indicate no significant dysregulated genes or low value of LFC (abs(LFC)<1). (J) Genes dysregulated in the Setdb1$^{MuSC-KO}$ cells in the "defense to virus" gene ontology analysis (n=2). (K) Western blot analysis of IRF3 (55 kDa), p-IRF3 (55kDa) and cGas (60 kDa) in Control and Setdb1$^{MuSC-KO}$ cells in vitro. (L) RT-qPCR of cytokines and interleukines found upregulated in the RNA-seq in Control and Setdb1$^{MuSC-KO}$ cells (n=3). Data are represented as mean ± SEM; $^{**}p < 0.01$, $^{***}p < 0.001$, $^{****}p < 0.0001$, t test.*

We next visualized the distribution of peak annotations between samples, and found an increased proportion of distal intergenic regions in *Setdb1$^{MuSC-KO}$*, where TE and ERVs are mostly located (Figure S4K). Through analyzing TEs specifically, we found around Transcription Start Site (TSS), localized in opened regions of the *Setdb1$^{MuSC-KO}$*, TEs that belong to different family such as DNA retrovirus, ERV1, ERVK, ERVL, or SINE (Figure 4G). Finally, the dynamic of chromatin accessibility around the different sub-families of ERV previously found showed an enrichment of the ATAC signal coverage on regions containing specific ERV in the *Setdb1$^{MuSC-KO}$* cells (Figure S4L-M). These results confirmed that the absence of SETDB1 modifies chromatin accessibility that induces the re-opening of ERV-containing regions.

DNA motif analysis on the promoter regions of genes upregulated in *Setdb1$^{MuSC-KO}$* cells identified binding motifs for FRA1, RUNX2 and CREB1, that were not present in *Control* cells (Figure S4N). These results indicate changes in the transcriptional regulators that control *Setdb1$^{MuSC-KO}$* cells and demonstrates that SETDB1 modulates chromatin through a dynamic process and compact chromatin on regions containing ERVs to silence their expression. Therefore, the absence of SETDB1 leads to the expression of ERV transcripts in MuSCs.

To understand the consequences of ERV de-repression in MuSC, we performed mass-spectrometry-based proteomics. We identified 260 significant deregulated proteins in *Setdb1$^{MuSC-KO}$* samples compare to the *Control* samples (Figure 4I; Table 3). Pathway analysis revealed enrichment for 'Interferon signaling' and 'Immune response' terms in *Setdb1$^{MuSC-KO}$* cells (Figure 4H). Interestingly, the most significantly abundant and significant pathways were 'Defense response to symbiont' and 'Defense response to virus' (Figure 4H). As ERVs, when re-expressed, can be detected as pathogens by their host cells[19], we further analyzed the upregulated proteins of these antiviral pathways and found several effectors of the cytosolic DNA-sensing pathway cGAS-STING pathway (Figure 4J). We confirmed increased phosphorylation of cGAS-STING downstream effector IRF3 in *Setdb1$^{MuSC-KO}$* cells compared to *Control* cells (Figure 4K, Figure S4O). cGAS-STING activation leads to the transcription of inflammatory cytokines. As such, RNA-seq and ATAC-seq analysis indicated a higher enrichment for 'Interferon' and 'Chemokine' pathways in *Setdb1$^{MuSC-KO}$* cells compared to *Control* cells (Figure 4A, Figure S4J). We further validated the increased expression of inflammatory cytokines in *Setdb1$^{MuSC-KO}$* cells using RT-qPCR (Figure 4L).

Taken together, multi-omics profiling indicates that *Setdb1* loss-of-function in MuSCs leads to chromatin opening at ERV loci. The subsequent re-expression of ancient viral elements activate cGAS-STING pathway and leads to aberrant cytokine expression by *Setdb1$^{MuSC-KO}$* MuSCs.

SETDB1 regulates MuSCs signaling toward inflammatory cells

To evaluate if aberrant cytokine expression by *Setdb1$^{MuSC-KO}$* MuSCs impact the whole muscle environment, we performed RT-qPCR for well-known genes involved in cytokine storm on tissue samples.[20] We found *Setdb1$^{MuSC-KO}$* muscles have higher expression of *Il10*, *Il6*, *Ifng*, *Ccl5*, *Ccl10*, *Ccl2* compared to *Control* muscles at 4 d.p.i. (Figure 5A) and at 7 d.p.i. (Figure 5B). We thus aimed to evaluate the impact of

inflammatory cytokine over-expression within the regenerating tissue. To this aim, we performed single-cell RNA-sequencing (scRNA-seq) on TA muscle extracts at 4 days post-injury.

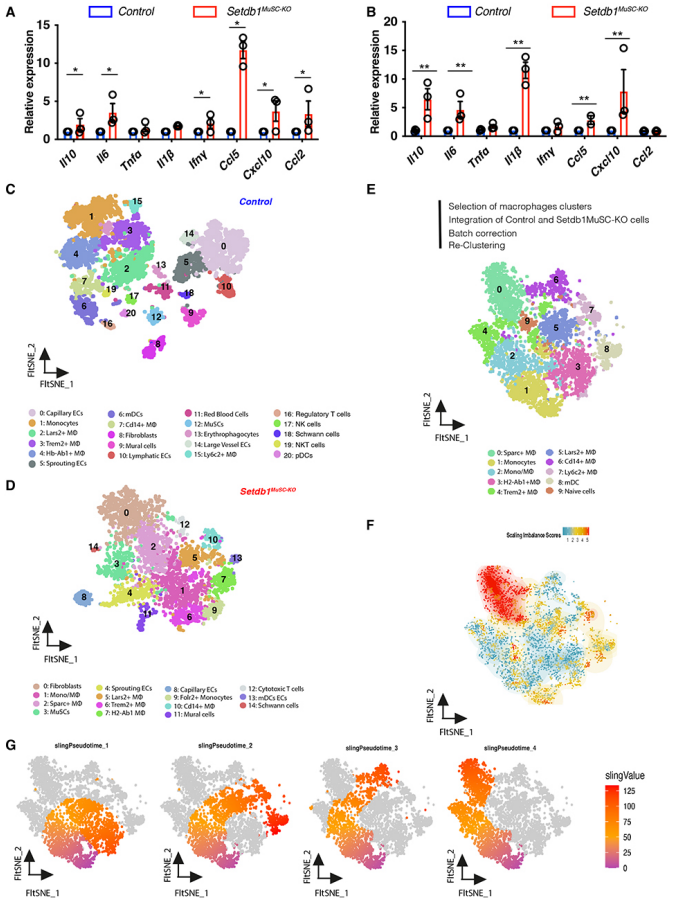

Figure 5. *A. RT-qPCR of cytokines and interleukines involved in cytokine storm in Control and Setdb1$^{MuSC-KO}$ TA (Tibialis Anterior) cryosections at 4 days after muscle injury using cardiotoxin (CTX). B. RT-qPCR of cytokines and interleukines involved in cytokine storm in Control and Setdb1$^{MuSC-KO}$ cells TA cryosections at 7 days after muscle injury (n=3). C. Single-cell transcriptome analysis of whole muscle in regeneration were isolated from CTX injured hind-limb muscles at 4 days post-injury, and subjected to scRNA-Seq using the 10x genomic platform. The different cell population were computed using Harmony + Louvain algorithm and projected on a FltSNE dimensional reduction, which identified 21 different clusters on separated sample analysis for Control samples (n=3 mice pooled in 1 sample). D. Single-cell transcriptome analysis of whole muscle in regeneration were isolated from CTX injured hind-limb muscles at 4 days post-injury, and subjected to scRNA-Seq using the 10x genomic platform. The different cell population were computed using Harmony + Louvain algorithm and projected on a FltSNE dimensional reduction, which identified 15 different clusters on separated sample analysis for Setdb1$^{MuSC-KO}$ samples (n=3 mice pooled in 1 sample). E. Single-cell transcriptome analysis of macrophages population from Control and Setdb1$^{MuSC-KO}$ samples Dataset were integrated by SCTtransform and different cell population were computed using Harmony + Louvain algorithm and projected on a FltSNE dimensional reduction, which identified 10 different macrophages clusters. F. Density mapping of Control and Setdb1$^{MuSC-KO}$ macrophages population whether nearby cells have the same condition of not. Red regions indicate specific population for the clusters 0 and 9 in Setdb1$^{MuSC-KO}$. Blue regions indicate equivalent proportion of population for each sample. G. Pseudotime trajectory using the Slingshot algorithm shows the cell trajectory in 4 projected lines across 10 clusters from the Fol2+ monocytes to the different populations of macrophages.*

Following normalization, quality control and random resampling, we selected 4,620 single cells for *Control* and for *Setdb1$^{MuSC-KO}$* muscles with an average of 1,629 genes expressed *per* cell in the *Control* condition and 1,271 for the *Setdb1$^{MuSC-KO}$*. The scRNA-seq data were analyzed using the R package Seurat.[21] We used unsupervised graph-based clustering[22] and embedded cells with FFT-accelerated Interpolation-based t-SNE (Flt-SNE). We annotated clusters to cell types based on differentially expressed genes and well-described canonical markers (Figure S5A, Figure S5B).

We found single cells from *Control* muscles to cluster adequately into 21 cell types, 12 of which were immune cells (Figure 5C). Among the non-immune cells, we found the excepted muscle-resident cells such as MuSCs, different types of Endothelial cells (ECs), Fibroblasts (containing both FAPs and Tenocytes) and Schwann cells. Remarkably, cell clustering was less efficient on single cells from *Setdb1$^{MuSC-KO}$* muscles. The cytokine storm within the tissue induced an inflammatory response signature by single cells and reduced the expression of cell-specific markers (Table 4). Furthermore, only 15 cell types were identified in the *Setdb1$^{MuSC-KO}$* dataset (Figure 5D). This shift in relative abundance is explained by enrichments of both Fibroblasts and Immune cells within *Setdb1$^{MuSC-KO}$* single cells. Most interestingly, while both samples contained similar macrophage subtypes (*Lars2+*, *Trem2+*, *H2-Ab1+*, *Cd14+*), *Setdb1$^{MuSC-KO}$* clustering revealed a population of intermediate Monocyte/Macrophage and a population of *Sparc+* macrophages (Figure 5D). We next validated the increase abundance of macrophages at 4 d.p.i. in *Setdb1$^{MuSC-KO}$* muscles by flow cytometry (Figure S5C) and immunostaining on tissue sections (Figure S5D). This augmentation was not associated with a shift in macrophage classical polarization (Figure S5E).

To study the cells appearing in *Setdb1$^{MuSC-KO}$* muscles, we selected the Monocytes and Macrophages from both datasets, integrated the single cells and clustered then anew (Figure 5E). We found 10 distinct populations, including the ones identified in both *Control* and *Setdb1$^{MuSC-KO}$* muscles, the *Sparc+* population, and a small cluster of cells that did not present any discriminating gene expression, which we named "naïve" (Figure 5E). To precisely map the contribution of each sample to the integrated dataset, we assigned a score to each single cell based on their origin. This scaling clearly identified the *Sparc^{+}* macrophages as a unique population specific to regenerating *Setdb1$^{MuSC-KO}$* muscles (Figure 5F). We next applied Slingshot to infer hierarchical trajectories onto the integrated macrophage populations.[23] We found four pseudotime lineages (Figure 5G), all arising from the monocyte cluster. Three of them give rise to populations present in both *Control* and *Setdb1$^{MuSC-KO}$* muscles and the fourth specifically gives rise to the *Sparc+* cluster. Pathway analysis on the macrophage clusters indicated the *Sparc+* cells have increased activation of Epithelial-Mesenchymal-Transition, Angiogenesis and Myc targets (Figure S5F). Differential gene expression analysis between the macrophage clusters further highlighted cell invasion and anti-viral signatures in *Sparc+* cells (Figure S5G).

Altogether, these data indicate that, in the absence of SETDB1, MuSCs will set off a cytokine storm within the regenerating muscle tissue. Consequently, *Setdb1$^{MuSC-KO}$* muscles undergo accumulation of immune cells. Among these appears a novel *Sparc+* macrophage lineage with pathological gene expression profile.

Macrophage histiocytosis and myofiber necrosis follow perturbation of the immune environment in Setdb1$^{MuSC-KO}$ muscles.

The identification of *Sparc+* antiviral macrophages in regenerating *Setdb1$^{MuSC-KO}$* muscles prompted us to have a closer look at tissue sections at timepoints following the appearance of these potentially pathological immune cells (Figure 6A). We observed an impressive 6-

fold increase in the macrophage marker F4/80 immunoreactive area in *Setdb1*$^{MuSC\text{-}KO}$ muscles compared to *Controls* at 7 d.p.i. (Figure 6B), Histological analysis of 10 d.p.i. muscles showed a more severe impairment of myofiber formation in *Setdb1*$^{MuSC\text{-}KO}$ muscles, compared to 7 d.p.i. (Figure 6B-C). Immunostaining for LAMIMIN highlighted a complete cellular disorganization of regenerating *Setdb1*$^{MuSC\text{-}KO}$ muscles as well as myofiber atrophy (Figure 6D-E).

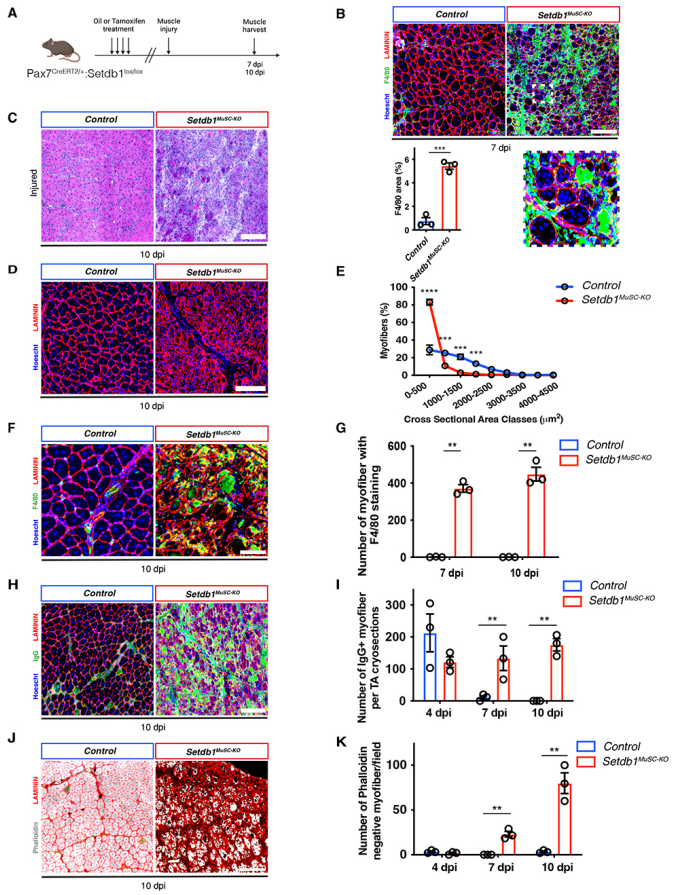

Figure 6. *(A) Experimental set up; Pax7*$^{CRE\text{-}ERT2}$*; Setdb1*$^{fl/fl}$ *mice intraperitoneally injected with either Oil or Tamoxifen. Cardiotoxin-induced injury (CTX) was performed in the TA (Tibialis Anterior) muscles and analyzed 10 post-injury. (B) F4/80 and LAMININ immunostaining in Control and Setdb1*$^{MuSC\text{-}KO}$ *muscles at 7 days after injury and quantification of the number of F4/80+ myofibers per field (n=3 mice).(C) Hematoxylin and eosin stain of TA muscle cross sections at 10 days post injury (CTX) (n=3 mice). (D) LAMININ immunostaining in Control and Setdb1*$^{MuSC\text{-}KO}$ *muscles at 10 days after injury (n=3 mice). (E) Distribution of cross-sectional area of CTX-injured TA muscles in Control and Setdb1*$^{MuSC\text{-}KO}$ *muscles (n=3 mice). (F) F4/80 and LAMININ immunostaining in Control and Setdb1*$^{MuSC\text{-}KO}$ *muscles at 10 days after injury and quantification of the number of F4/80+ myofibers per field (n=3 mice). (G) Quantification of the number of myofibers with F4/80 immunostaining in the Control and Setdb1*$^{MuSC\text{-}KO}$ *muscles at 7 and 10 days post injury (n=3 mice). (H) IgG immunostaining in Control and Setdb1*$^{MuSC\text{-}KO}$ *muscles at 10 days after injury (n=3 mice). (I) Quantification of the number of IgG+ myofiber per cryosections in the Control and Setdb1*$^{MuSC\text{-}KO}$ *muscles at 4, 7 and 10 days post injury (n=3 mice). (J) Phalloidin immunostaining in Control and Setdb1*$^{MuSC\text{-}KO}$ *muscles at 10 days after injury (n=3 mice). (K) Quantification of the number of IgG+ myofiber per cryosections in the Control and Setdb1*$^{MuSC\text{-}KO\ \Delta}$ *muscles at 4, 7 and 10 days post injury (n=3 mice). Data are represented as mean ± SEM;* $^{**}p < 0.01$, $^{***}p < 0.001$, $^{****}p < 0.0001$*, t test. Scale bars, (B) 150 µm (C) 50 µm (D) 100 µm (F) 25 µm (H) 125 µm (J) 50 µm*

By evaluating both F4/80 and LAMININ immunostainings at 10 d.p.i. (Figure 6F), we observed that macrophages were almost absent in control regenerated muscles, while they massively invade myofibers in *Setdb1*$^{MuSC\text{-}KO}$ muscles (Figure 6G). These data demonstrate that the hypercytokinemia triggered by the loss of SETDB1 in MuSCs results in macrophage histiocytosis.

Macrophage puncture into myofibers happens following acute damage to clean out the tissue from degenerating cells, but also in some inflammatory myopathy in which the diffuse infiltration of macrophages causes myofiber damage.[24] We then performed IgG immunostaining at 7 d.p.i. and 10 d.p.i. to evaluate myofiber integrity (Figure 6H). We also stained 4 d.p.i. muscles as an internal control of the experiment, since necrotic myofibers are present following CTX injury in *Control* regenerating muscles. Almost no IgG+ myofibers were detected in control regenerating muscles at 7 d.p.i. and at 10 d.p.i., yet *Setdb1*$^{MuSC\text{-}KO}$ muscles exhibited high numbers of permeable myofibers at these time points (Figure 6I). As myofibers undergoing necrosis break their sarcomeres down, we stained sections with phalloidin to reveal filamentous ACTIN (f-ACTIN) (Figure 6J). While the entirety of myofibers in control muscles showed homogeneous f-ACTIN expression at all time points, we found f-ACTIN-negative myofibers in *Setdb1*$^{MuSC\text{-}KO}$ muscles at 7 d.p.i. and an increased amount of these necrotic myofibers at 10 d.p.i. (Figure 6K).

Taken together, these observations imply that regenerating *Setdb1*$^{MuSC\text{-}KO}$ muscles undergo histiocytosis, penetrance of macrophages into newly formed myofibers and their subsequent necrosis. This phenomenon correlates with the complete absence of regenerated myofibers within *Setdb1*$^{MuSC\text{-}KO}$ muscles at 28 d.p.i., while new myofibers (albeit poorly formed) are present at earlier timepoints following injury.

SETDB1 is not essential for muscle resident mesenchymal progenitors

Lastly, we investigated if targeted *Setdb1* gene disruption in another muscle-resident progenitor cell type, the FAPs, has a similar impact on regeneration as in MuSCs. To this aim, we crossed the *Setdb1* floxed mice with mice with CreERT2 inserted into the start codon of the *Pdgfra* gene.[25] We used the same tamoxifen-inducible recombination protocol for the *Pdgfrα*$^{CreERT2/+}$:*Setdb1*$^{lox/lox}$ mice as the one for the *Setdb1*-cKO mice, and we then performed CTX injury (Figure 7A).

At 7 d.p.i, we did not observe any difference between genotypes in terms of muscle weights (Figure 7B) and muscle histology on cross-sections (Figure 7C). Likewise, MuSC quantification at 7 d.p.i. did not reveal any impact of FAP-specific *Setdb1* gene disruption (Figure 7D).

Furthermore, both the number and size of the eMyHC+ regenerating myofibers were similar between genotypes (Figure 7E-F). Strikingly, targeted *Setdb1* gene disruption in FAPs neither impacted connective tissue remodeling nor promoted macrophage accumulation in the regenerating muscle (Figure 7H-I). These results demonstrate that *Setdb1* expression is dispensable in FAPs during muscle regeneration.

Finally, we purified FAPs from uninjured muscles of *Pdgfrα*$^{CreERT2/+}$:*Setdb1*$^{lox/lox}$ mice that were treated with Tamoxifen or corn oil *in vivo*. We confirmed efficient *Setdb1* gene deletion in purified cells (Figure S6A, Figure S6B). We did not observe any difference of the percentage of EdU^{+} cells between control and *Setdb1*$^{FAP\text{-}KO}$ FAPs after 4 days *in vitro* (Figure 7J, Figure S6C). Interestingly, we probed for the expression of the cytokines that were over-expressed by *Setdb1*$^{MuSC\text{-}KO}$ MuSCs and did not find any differences in these genes' expression levels between *Control* FAPs and *Setdb1*$^{FAP\text{-}KO}$ FAPs (Figure 7K). Lastly, *Setdb1*$^{FAP\text{-}KO}$ cells did not show activation of the cGAS-STING pathway (Figures S6D, Figure S6E).

Taken together these data show that, in contrary to MuSCs, SETDB1 has no major role in FAPs and its absence does not result in cytokine storm *in vivo*.

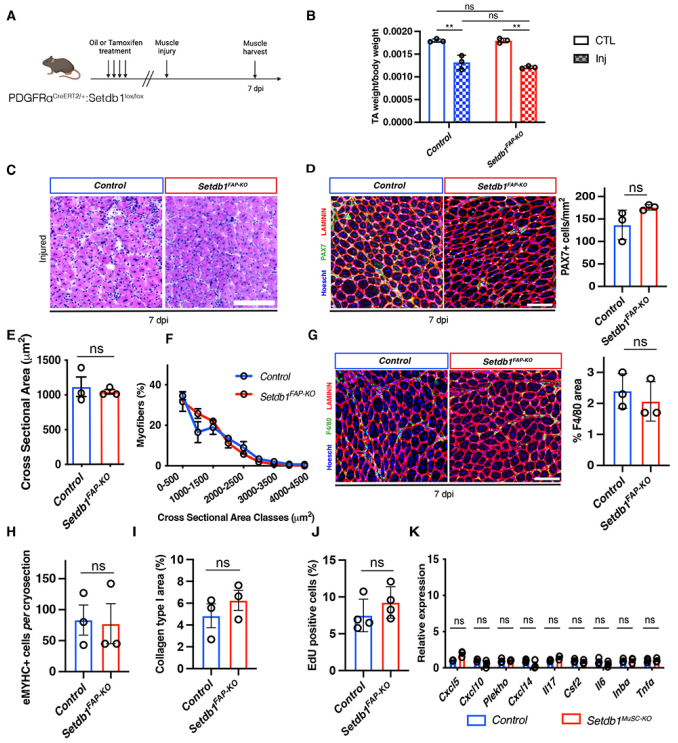

Figure 7. *(A) Experimental scheme; PDGFRα$^{CRE-ERT2}$; Setdb1$^{fl/fl}$ mice intraperitoneally injected with either Oil or Tamoxifen and cardiotoxin (CTX) is performed on TA (Tibialis Anterior) muscle after 28 days post injury. (B) Normalized TA weight on mice body weight represented in Control and Setdb1^{FAP-KO} conditions in uninjured and injured TA (n=3 mice). (C) Hematoxylin and eosin stain of TA muscle cross sections at 7 days post injury (CTX) (n=3 mice). (D) Immunostaining for LAMININ and PAX7 on TA cryosections 7 days after injury and quantification of the number of PAX7+ cells on TA cryosections (n=3 mice). (E) Cross sectional area of CTX-injured TA muscles of Control and Setdb1^{FAP-KO} muscles after 7 days post injury (n=3 mice). (F) Distribution of cross-sectional area of CTX-injured TA muscles of Control and Setdb1^{FAP-KO} condition after 7 days post injury (n=3 mice). (G) F4/80 and LAMININ immunostaining in Control and Setdb1^{FAP-KO} muscles at 7 days after injury and quantification of the number of F4/80+ myofibers per field (n=3 mice). (H) eMYHC+ myofiber per cryosection in Control and Setdb1^{FAP-KO} muscles at 7 days after injury (n=3 mice). (I) COLLAGEN I area quantification on TA cryosections 28 days after injury in Control and Setdb1^{FAP-KO} conditions (n=3 mice). (J) Quantification of EdU+ cells in Control and Setdb1^{FAP-KO} cells in vitro (n=3). (K) RT-qPCR on cytokines and interleukins in Control and Setdb1^{FAP-KO} cells in vitro (n=3). Data are represented as mean ± SEM; n.s not significant, $^{**}p < 0.01$, t test. Scale bars, (C) 120 µm (D) 80 µm (G) 80 µm.*

Discussion

In this study, we describe for the first time a role for the histone lysine methyl transferase SETDB1 in adult muscle stem cells in a regenerative context. Our data show that SETDB1 is required for MuSCs fate and plays an essential role to ensure proper muscle regeneration. Mechanistically, SETDB1 represses a specific family of transposable elements in MuSCs, the ERVs. This repression prevents the transcription of these viral portions of the genome that will lead to MuSCs proliferation arrest and cell death. Unexpectedly, we also found that ERVs de-repression in MuSCs also affects muscle environment. Indeed, activation of cGAS-STING pathway in MuSCs will entail interferon and chemokines release, stimulating a massive inflammation and a cytokine storm inside the whole muscle leading to the complete abolition of the regeneration. Therefore, our work identified a crucial role for SETDB1 in protecting muscle regeneration in response to injury and inflammation.

Transposable Elements (TEs) are genetic elements with the ability to replicate and transpose within the genome of germline and specific somatic cells.[26] Close to 40% of the mouse genome is made up of fossils of transposable elements. Of which approximately 10% represent endogenous retrovirus (ERV) sequences. These ERV sequences have resulted from both ancient and modern infections by exogenous retroviruses, which have successfully colonized the germ line of their host. ERVs are clearly detrimental to their hosts but are also important functional components of the genome. As such, opposing mechanisms must be set in place to mitigate their effects as well as to maintain their presence and function. As observed in our work, muscle cells express ERVs at the basal level. These ERVs can induce insertional mutations that are found mostly in introns, with no negative effects. However, ERVs have been studied and found upregulated and disastrous in context of cancer, autoimmune diseases and neurodegenerative pathologies. Their functions and especially the consequences of their re-expression have not previously been studied in the context of adult tissue regeneration. Previously, a role for ERVs had been established in skeletal muscle, as they may be involved in statin-induced myopathies.[27,28] In contrast, our results indicate that when MuSCs are activated from quiescence upon injury, ERVs de-expression have more severe consequences, and leads to complete disaggregation of regenerating muscle fibers. We suggest that active repression of ERVs in muscle cells is a crucial process to allow for normal muscle physiology.

The cGAS-STING cytosolic DNA-sensing pathway and its link with inflammation has been extensively studied these past years.[29–31] Many studies highlighted the activation of the pathway in an anti-viral response context. In addition, cGAS-STING is involved in anti-proliferative process and cell death, notably in mouse embryonic fibroblasts (MEFs) and HeLa cells.[32–34] We observed that *Setdb1-null* MuSCs undergo cell cycle arrest and cell death concomitantly to cGAS-STING pathway activation. Our results bring for the first time the answer of how adult somatic stem cells respond to cGAS-STING activation. Importantly, the link between Setdb1 and the cGAS-STING pathway has been described in two recent studies performed in cancer cells, showing that absence of SETDB1 leads to ERV de-repression and cGAS-STING activation but they also demonstrated how SETDB1 can be used as therapeutic target.[17,18] Here, we show that the activation of the cGAS-STING pathway in *Setdb1-null* MuSCs results in hypercytokinemia and histiocytosis of the regenerating tissue. Our findings demonstrate that in a non-cancerous and non-pathological context, this aberrant inflammatory response will abolish muscle repair with no compensation mechanism, leading to widespread tissue destruction.

We found the aforementioned dysregulation in regenerative inflammation results from interferons and cytokines release linked to cGAS-STING activation. Interestingly, cGAS-STING has already been described to be involved in several cases of cytokine storm, notably in SARS-CoV-2 context.[35] The production of interferons and cytokines is turned on by NF-κB and IRF3/TBK1 signals, attracting numerous immune cell types and especially macrophages that will contribute to the cytokine storm and maintain inflammation. Interestingly, a recent paper already suggested SETDB1 may be an actor in cytokine storm cascade.[36] Here, we experimentally created, for the first time, a cytokine storm in adult skeletal muscle. The results presented in this paper, alongside with

the multi-omics datasets we provide, may bring insights in the consequential effect of SARS-CoV-2 infection on skeletal muscle function. While the effect of this virus and its associated cytokine storm in susceptible human populations on skeletal muscle homeostasis and function is still being explored, its functional receptor ACE2 (Angiotensin Converting Enzyme 2) is strongly expressed by muscle cells.[37] As such, it is conceptualizable that a decline in skeletal muscle excitability and strength may contribute to the decreased respiratory efficiency in patients with COVID19, since the diaphragm is one of the essential components of the respiratory system and is indispensable to maintain lung capacity.[38,39]

Further to that point, our results show that proliferating *Setdb1-null* MuSCs, with active cGAS-STING pathway, will act as a strong attractant for macrophages to the site of muscle injury. These *Sparc*+ macrophages do not present the same characteristic as the healthy macrophages required for efficient muscle regeneration.[40] The inflammatory cytokines released by *Setdb1-null* MuSCs are known to influence monocyte polarization into either pro- or anti-inflammatory macrophages, notably in cancer.[41,42] Similarly, the cGAS-STING pathway has been shown to be related to the acquisition of tumor-associated-macrophage (TAMs) phenotype.[43,44] TAMs are well described as a dysregulated immune cell population involved in tumor growth and metastasis and demonstrating an aggressive behavior *in vivo*.[45] Strikingly, the *Sparc*+ macrophages we found only in *Setdb1*-cKO muscles have TAM characteristics such as matrix formation (expression of cathepsins, and collagens) and epithelial-mesenchymal-transition. Thus, we conclude SETDB1 is required, in adult MuSCs, for their proper communication with reparative immune cells.

While there is no evidence, so far, implicating SETDB1 in a skeletal muscle pathology, some previous studies demonstrated that myofibers invasion by immune cells and notably by macrophages can be observed in different contexts of Inflammatory Myopathy with Abundant Macrophages (IMAM).[46,47] The causes of IMAM are still unknown and needs to be investigated, but the presence of macrophages inside myofibers in these diseases may relates to our findings, Interestingly, a recent publication demonstrated that IMAM and other rare idiopathies and myopathies could be related to the cGAS-STING pathway.[48] Strikingly, it is crucial to go deeper in the understanding of these pathologies.

Finally, we found that targeted deletion of *Setdb1* in FAPs does not affect these cells' proliferation capacities, as well as the muscle regeneration process following acute injury. This discrepancy with MuSCs can be explained by a divergence in the actors dedicated to histone methylation by these different muscle-resident progenitor types. Interestingly, targeted disruption of another H3K9 methyltransferase, G9a (KMT1C), in MuSCs has no effect on muscle regeneration.[49] In contrast, G9a has recently been shown to be required for the maintenance of FAPs identity *in vivo*[50]. Taken together, these observations clearly indicates that different stem/progenitor cell types within a given tissue have unequal requirements for specific KMTs. One can also expand this concept to propose that different stem/progenitor cell may have divergent needs for TE silencing. Indeed, H3K9 KMTs favors different TE classes, like SUV39H1 (KMT1A) which represses class II ERVs, such as the intracisternal A-particles (IAPs), but also the long interspersed nuclear elements (LINEs) such as LINE1 in mESCs[51] while SETDB1 is known to be recruited for the repression of the class I and II of Long terminal repeat (LTR) and IAPs in mESCs.[16] Therefore, our results advocate that SETDB1 may be an important regulator of adult stem cell function in general, but depending on the tissue or the cell type other H3K9 KMTs should be considered.

In conclusion, we identified the H3K9 KMT SETDB1 to be required for ERVs silencing in adult MuSCs, but not FAPs. Through preventing unscheduled ERV expression during MuSCs following activation from quiescence, SETDB1 allows for their amplification and proper communication with the regenerative inflammatory cells preventing histiocytosis and myofiber necrosis (Figure 8). These findings represent a significant advance in our understanding of MuSCs biology and muscle regeneration. Further work will investigate the role of SETDB1 in context of pathologies such as inflammatory myopathies and of sarcopenia due to aging.

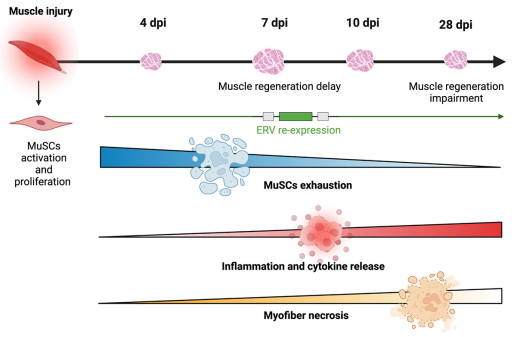

Figure 8. A proposed model for the lack of regeneration in *Setdb1*$^{MuSC\text{-}KO}$ *muscles*

Materials and Methods

Mice Lines

Animals were handled according to the European Community guidelines, implementing the 3Rs rule. Protocols were validated by the ethic committee of the French Ministry, under the reference number APAFIS#34582-202111121631816 v3. All mice were kept under pathogen-free conditions with a 12 h/12 h light/dark cycle.

All *in vivo* experiments were performed on male mice of 10 weeks old. Generation and genotyping of the Pax7^{CreERT2}, Setdb1$^{lox/lox}$ and PDGFRα^{CreERT2} lines have been described previously. These strains were used to generate combined experimental strains, which include the Setdb1$^{fl/fl}$ Pax7^{CreER}, Setdb1$^{fl/fl}$ and PDGFRα^{CreERT2} strains described.

Generating combined strains was performed through breeding of homozygous parental strains (F0) to generate a heterozygote population (F1), which was crossed amongst itself to generate the desired homozygous strain (F2). Genotyping was performed throughout to assure the desired genotype. Housing was performed with 2 females with 1 male.

Tamoxifen injection and muscle injury

To induce the Cre activity, four consecutives intraperitoneal (IP) injection of tamoxifen were administrated to the 2 months old mice (100µL at 10mg/mL dissolved in corn oil). The cardiotoxin injury was performed 7 days after the first injection of tamoxifen. Mice were anesthetized with isoflurane inhalation. The injury was induced by 50µL intramuscular injections of cardiotoxin (CTX; 10µM) in the *Tibialis Anterior* (TA) muscle.

Isolation of Tibialis Anterior and Histological analysis

Mice were euthanized with CO_2 asphyxiation and cervical dislocation. TA muscles were harvested from the hindlimbs, weighed, submerged in OCT and then frozen in isopentane cooled in liquid nitrogen. Frozen muscles were stored at -80°C. 10µm muscle sections thickness was collected. Fixation of muscle section was performed with 4% PFA/PBS during 10 minutes at room temperature. Permeabilization was done in 0.1M glycine, 0.1% Triton X-100 diluted in PBS during 10 minutes at room temperature. After 3 washes in PBS, Muscle section were incubated with blocking buffer (3% BSA, 0.1% Triton X-100, in PBS)

during 1 hour containing 2% BSA diluted in PBS supplemented with M.O.M. Blocking reagent. Primary antibodies diluted in blocking buffer were incubated overnight at 4°C. Detection of primary antibodies was achieved using Alexa Fluor secondary antibody at a 1:1000 in blocking buffer after 3 times washes in PBS. Nuclei were counterstained with Hoechst at 1µg/mL in PBS before mounting with fluorescent mounting medium. Full muscle section was taken on a slide scanner ZEISS AxioScan7. Images were processed and analyzed with ZEISS ZEN and FIJI software.

Murine cell cultures

Skeletal muscle-derived primary myoblasts were isolated from the different mice model between 8- to 16-week-old using the magnetic cell separation (MACS® miltenyi). Hindlimbs muscles from both legs were dissected and places in a sterile Petri dish containing PBS. Mechanic dissection was performed with scissors to have a pulp of muscle. The pulp was digested in a bath of Collagenase II solution diluted in Ham's F10 Nutrient Mix during 1 hour at 37°C. A second digestion is performed during 30 min containing Collagenase II and Dispase at 37°C. The pulp is then filtered (70µm and 30µm) followed by a step of trituration using syringe 0.2G. Washes were done with 5% Bovine Serum Albumin (BSA), 3mM EDTA diluted in phosphate buffered saline (PBS) and myoblasts isolation was performed using Satellite Cell Isolation kit. The cell suspension is then poured into Columns in the magnetic field (LD Column, Miltenyi). Unlabeled cells (satellite cells) flow through the column while magnetically labeled cells are retained within the column. Satellite cells were resuspended in the growth medium (Ham's F10 with 20% FBS, 1% Penicillin/Streptomycin (P/S)), and 2.5 ng/mL of basic fibroblast growth factor and plated into a collagen-coated 60mm Petri dish. Cells were maintained in the growth medium until cells reached 80% confluence.

Immunostaining on cell and myofibers

Cell fixation was performed with 4% PFA/PBS during 10 minutes at room temperature and 3 washes in PBS were done before permeabilization step. Permeabilization was done in 0.1M glycine, 0.1% Triton X-100 diluted in PBS during 10 minutes at room temperature. If cells or myofibers were pre-incubated with EdU, the Click-iT reaction was done using the Click-iT EdU Alexa Fluor 647 Imaging kit according to the manufacturer's protocol. After 3 washes in PBS, Muscle section were incubated with blocking buffer during 1 hour. Primary antibodies diluted in blocking buffer were incubated overnight at 4°C. Detection of primary antibodies was achieved using Alexa Fluor secondary antibody at a 1:1000 in blocking buffer after 3 times washes in PBS. Nuclei were counterstained with Hoechst at 1µg/mL in PBS.

Single myofiber isolation

Single myofiber isolation was performed using *Extensor Digitorum Longus* (EDL) muscle and using the previous method published.[52] EDL were harvested from tendon to tendon and digested for 1 hour in DMEM containing 0.25% collagenase II. After digestion, muscle trituration and washes are performed in DMEM. Isolated myofibers were cultured in 20% fetal bovine serum, 1% P/S. After 24 hours or 72 hours in culture myofibers were fixed using PFA 4% diluted in PBS.

RNA extraction, cDNA synthesis and RT-qPCR

A minimum of 2 x 10^5 cells were collected per sample for RNA extraction using the Nucleospin RNA II kit following the manufacturer protocol. Reverse transcription was performed using the SuperScripts III Reverse Transcriptase. RT-qPCR was performed using SYBR Green. The relative mRNA levels were calculated using the $2^{-\Delta\Delta Ct}$ method. The ΔCt were obtained from Ct normalized to the housekeeping genes *Gapdh* and *Hprt* levels in each sample. The RT-qPCR primers used are listed in the Supplementary Table 2.

Cell death experiment

Myoblasts were cultured in 100mm Petri dish and then treated with either ethanol or 4-hydroxytamoxifen during 5 days. Cells were trypsinized and resuspended in PBS 50µg/mL of Propidium iodide were added during 30 min at 37°C. After 2 washes, 1µM/mL of YO-PRO-1 were added in PBS during 1 hour in ice. After 2 washes in PBS, cells were analyzed with a flow cytometer BD FACSCanto™ II.

Cell cycle experiment using flow cytometry

Myoblasts were cultured in 100mm Petri dish and then treated with either ethanol or 4-hydroxytamoxifen during 5 days. At least 1x10^5 cells were fixed with 70% ethanol diluted in cold PBS. Cells were centrifuge and the pellet was resuspended in 1mL of PBS containing 0.1mg/mL of RNAse A and 50µg/mL of Propidium iodide overnight at 4°C. After 2 washes in PBS, cells were analyzed with a flow cytometer BD FACSCanto™ II.

Muscle dissection and satellite cell isolation

FACS-isolation of satellite cells was performed following: Muscles were dissected, minced, and incubated in digestion buffer: 2 µg/mL Collagenase II during 1 hour, and 3.25µg/mL Dispase II for 30 min at 37°C, and purified by filtration using 70µm and 30µm cell strainers after trituration with 0.2 syringe. Cell suspensions were incubated 30 min on ice with the following antibodies: anti-ITGA7, anti-CD34, anti-CD45, Anti-CD106 and anti-Ly-6/E (SCA1) (Supplementary Table 1). Cells were sorted by gating CD34 + ITGA7+ double positive lineage.

RNA-sequencing of satellite cells

RNA was prepared as described for RNA extraction and sent to the Genom'IC (Institut Cochin) genomic platform. Libraries were prepared with TruSeq Stranded Total Library preparation kit according to supplier recommendations. The important steps of this protocol are the removal of ribosomal RNA fraction from 400ng of total RNA using the Ribo-Zero Gold Kit; fragmentation using divalent cations under elevated temperature to obtain ~300 bp pieces; double strand cDNA synthesis using reverse transcriptase and random primers, and finally Illumina adapters ligation and cDNA library amplification by PCR for sequencing. Sequencing was carried out on pair-end 75 bp of Illumina NextSeq® 500.

RNA-sequencing analysis

Nf-core/rnaseq v3.2 was used on a conda container, the raw fastq reads aligned with STAR and to project the alignments onto the transcriptome and to perform the downstream BAM-level quantification with Salmon. Data were filtered to conserve only features in canonical chromosomes (1 to 19, X, Y and mitochondrial) identified as protein coding in Ensembl databases. Differential analysis was performed with DEseq2 package (v1.34.0). Gene set enrichment analysis was computed by fgsea package (v1.20.0) on genes ranked by the sign of Log2 Fold Change * log10(p-adjusted by BH). The gProfiler2 package (v.0.2.1) was used to compute and compare multiple input collections from MH, M2:CP, KEGG, M5:GO on genes ranked by the sign of Log2 Fold Change * log10(p-adjusted by BH).

ATAC-sequencing of MuSCs

MuSCs were extracted as described in the "murine cell culture". MuSCs were plated at 10 000 cells/cm^2 and treated during 3 days with either ethanol or 4-hydroxitamoxifen. Cells were tryspsinized, frozen and sent to the Diagenode platform in Belgium for sequencing.

ATAC-sequencing analysis

Nf-core/atacseq v1.2.1 was used on a docker container and in standard parameters to compute a rds archive readable in R and different files in multiple formats (bigwig, bed, bam). Data were filtered to conserve only features in canonical chromosomes (1 to 19, X, Y and mitochondrial). To determine chromatin occupancy, bam files were parsed and only reads paired were conserved, properly paired and MAPQ score = 60 with Rsamtools package (v2.10.0). Differential analysis was performed on count reads over regions from peak calling with DEseq2 package (v1.34.0). To facilitate reading, coverage by chromosome was computed, log-transformed coverage scores and plotted only value>3.1 into a circos plot with circlize package (v.0.4.15).

Mass spectrometry-based proteomics

Primary myoblasts were treated with ethanol or 4-OHT as described above in the 'murine cell culture'. The cells were thawed and then lysed by RIPA buffer (50 mM Tris-HCl pH7.4, 150 mM sodium chloride, 1 mM EDTA, 0.1% sodium dodecyl sulfate, 1% Triton X-100, 1.5% sodium deoxycholate). Proteins in cell lysates were precipitated by 4 volumes of pre-cooled acetone (Honeywell). The precipitated proteins were sent to the Proteomics core of Biosciences Central Research Facility, HKUST (Clear Water Bay), for subsequent processing. The protein pellets were washed sequentially with pre-cooled acetone, pre-cooled ethanol, and pre-cooled acetone. Sample preparation for mass spectrometry, including protein treatments and clean-up, was done using the iST PreON 96x kit (PreOmics). The samples were loaded onto Bruker timsTOF Pro mass spectrometer. A detailed description of the mass spectrometer is given in ref[53]. The operation parameters had been listed previously[54]. The accumulation and ramp time were set at 100 ms each. The mass spectra were recorded using positive electrospray mode, in the m/z range of 100-1700. The ion mobility was scanned from 0.85-1.35 Vs cm-2. The overall acquisition cycle was 0.53 s, comprising one full TIMS-MS scan and four Parallel Accumulation-Serial Fragmentation (PASEF) MS/MS scans. The TIMS dimension was calibrated linearly using three selected ions from the Agilent ESI LC/MS tuning mix [m/z, 1/K0: (622.0289, 0.9848 Vs cm−2), (922.0097, 1.1895 Vs cm−2), (1221,9906, 1.3820 Vs cm−2)] in positive mode.

Mass spectrometry analysis

The raw data were processed by PEAKS software (version: Xpro). The database for protein search was Uniprot. The taxonomy for protein search was Mus musculus. The parent ion tolerance was 15 ppm, and the fragment ion tolerance was 0.06 Da. The protein FDR was 1%.

For label-free quantification of the mass spectrometry data, normalized spectral abundance factor (NSAF)-based spectral counting method[55] was used here. The NSAF method can account for the influence of protein sizes on spectral counts and normalize the total spectral counts across multiple samples. Briefly, spectral abundance factor (SAF) of each protein was obtained by dividing the spectral count with its protein length. Then, NSAF was calculated by dividing the SAF with the total SAF of each sample. Since NSAF values were small, the normalized data were multiplied and presented as NSAF*1000000. To examine differential expression of proteins between control and knockout samples, unpaired two-tailed Student's t-test was used, assuming equal variance of the two groups. Statistical significance was set at unadjusted $p < 0.05$.

Sample preparation for Single-cell RNA-sequencing

Mice were injected with either corn oil or Tamoxifen and CTX injections on TA were done 7 days after the last injection. After 4 days, TA muscles were dissected, minced, and incubated in digestion buffer: Ham's F-10 Nutrient Mix, 2µg/mL Collagenase II for 1 hour, and Collagenase II and 3.25µg/mL Dispase for 30min at 37 °C, and purified by filtration using 70µm and 30µm cell strainers (Miltenyi Biotec). Cells were stained with Hoechst and Single-cell RNA sequencing was done at the genomic platform from the CRCL using 10X genomic.

Single-cell RNA sequencing

Data demultiplexed in fastq format was check with fastqc and fastq_screen to control quality sequencing. Sequencing reads were processed with STAR (v.2.7.8a) to align and count data for each sample. The downstream analysis was carried to Seurat package (v.4.0.1). Each of the 4 datasets was first analyzed independently before combining datasets. Features in canonical chromosomes (1 to 19, X, Y and mitochondrial), identified as protein coding in Ensembl databases and expressed at minimum in 10 "cells" were conserved. To compare with others resources, different empiric limitedness from publications used to analyze data from similar single cell experiments on the same whole tissue (800 – 10k counts RNA ; 600 – 6000 features RNA ; 5% Mitochondrial part). DropletUtils (v.1.14.2) to compute barcode rank statistics and identify knee and inflexion points on the total count curve. Cells were selected when their ranks are between high "empiric" thresholds (10k) and knee plot value for each sample, others cell ranks are rejected. After filtering, metrics were recalculated. For each sample, SCTransform and RunPCA from Seurat package performed to allow used DoubletFinder (v.2.0.3) and to identify and to remove cell doublets. The optimal dimension threshold from PCA results were determined by a custom method. Before integration, each sample was log-normalized on top2000 features by the vst algorithm. After identifying anchors and performing integration, data were scaled using a linear model. After integration, RunPCA and RunHarmony from the Seurat package were calculated; for both, the optimal dimension threshold was determined by a custom method. The optimal dimension threshold from PCA was used to calculate Harmony reduction. The optimal dimension threshold from Harmony used to compute the Shared Nearest-neighbor graph. Original Louvain algorithm with 0.7 resolution performed to determine clusters. Reduction dimension graphs were generated by RunTSNE which uses FFT-accelerated Interpolation-based t-SNE (Flt-SNE). Markers of gene expression for each cluster were found by MAST and ROC analysis methods for all features and with no filters (min.pct=0 ; logfc.threshold=-Inf ; only.pos=F; densify=T). Slingshot (v.2.2.1) was used to calculate trajectories. Imbalance_score function (modify for own needs) was used to compute an imbalance score to show whether nearby cells have the same condition of not and progressionTest function from Condiment package for both (v.0.99.14) was used to compute a test whether or not the pseudotime distribution are identical within lineages between conditions. TradeSeq package (v.1.8.0) was used to allow analysis of gene expression along trajectories.

Statistical analysis

A minimum of three biological replicates was performed for the presented experiments. Error bars are standard errors. Statistical significance was assessed by the Student t test, using Microsoft® Excel® and GraphPad Prism 9. Differences were considered statistically significant at the $P < 0.05$ level. For each sample, four images were taken with a ×4, ×10, or ×20 magnification depending on the experimental design. Cell and western blot quantification and analysis were performed using ImageJ.

End Matter

Author Contributions

F.L.G conceived the study, designed the project, and obtained grant funding. F.L.G supervised the project and managed the laboratory. P.G performed most of the experiments. W.J performed bio-informatic analyses. C.B. performed single myofiber experiments and helped P.G with in vivo experiments. L.G performed preliminary experiments. C.P setup the mice colony and performed preliminary experiments. F.L.G. performed scRNA-seq. F.A performed cell culture experiments. W.K and T.C performed proteomics. P.G, T.C and F.L.G designed or interpreted experiments. P.G and F.L.G wrote the manuscript. All authors reviewed and edited the manuscript.

Acknowledgments

The research conducted in the Le Grand lab was supported by funding from the Inserm, the CNRS, the Agence National pour la Recherche (ANR-19-CE13-0016, ANR-17-CE12-0010-02), the Association Française contre les Myopathies/AFM-Téléthon and the European Joint Program for Rare Diseases (EJPRD JTC2019, Myocity project). C.B. was supported by a post-doctoral fellowship from the Fondation pour la Recherche Médicale (FRM). The authors acknowledge the PLATIM and CIQLE microscopy facilities of Université Claude Bernard Lyon 1. We thank C. Degletagne of the Plateforme Génomique des Cancers for support with single cell RNA-seq.

References

1. Zakrzewski, W., Dobrzyński, M., Szymonowicz, M., and Rybak, Z. (2019). Stem cells: past, present, and future. Stem Cell Res Ther 10, 68. 10.1186/s13287-019-1165-5.

2. Janssen, S.M., and Lorincz, M.C. (2022). Interplay between chromatin marks in development and disease. Nat Rev Genet 23, 137–153. 10.1038/s41576-021-00416-x.

3. Schultz, D.C., Ayyanathan, K., Negorev, D., Maul, G.G., and Rauscher, F.J. (2002). SETDB1: a novel KAP-1-associated histone H3, lysine 9-specific methyltransferase that contributes to HP1-mediated silencing of euchromatic genes by KRAB zinc-finger proteins. Genes Dev 16, 919–932. 10.1101/gad.973302.

4. Bilodeau, S., Kagey, M.H., Frampton, G.M., Rahl, P.B., and Young, R.A. (2009). SetDB1 contributes to repression of genes encoding developmental regulators and maintenance of ES cell state. Genes Dev 23, 2484–2489. 10.1101/gad.1837309.

5. Ceol, C.J., Houvras, Y., Jane-Valbuena, J., Bilodeau, S., Orlando, D.A., Battisti, V., Fritsch, L., Lin, W.M., Hollmann, T.J., Ferré, F., et al. (2011). The histone methyltransferase SETDB1 is recurrently amplified in melanoma and accelerates its onset. Nature 471, 513–517. 10.1038/nature09806.

6. Zakharova, V.V., Magnitov, M.D., Del Maestro, L., Ulianov, S.V., Glentis, A., Uyanik, B., Williart, A., Karpukhina, A., Demidov, O., Joliot, V., et al. (2022). SETDB1 fuels the lung cancer phenotype by modulating epigenome, 3D genome organization and chromatin mechanical properties. Nucleic Acids Research 50, 4389–4413. 10.1093/nar/gkac234.

7. Yin, H., Price, F., and Rudnicki, M.A. (2013). Satellite cells and the muscle stem cell niche. Physiol. Rev. 93, 23–67. 10.1152/physrev.00043.2011.

8. Porpiglia, E., and Blau, H.M. (2022). Plasticity of muscle stem cells in homeostasis and aging. Current Opinion in Genetics & Development 77, 101999. 10.1016/j.gde.2022.101999.

9. Beyer, S., Pontis, J., Schirwis, E., Battisti, V., Rudolf, A., Le Grand, F., and Ait-Si-Ali, S. (2016). Canonical Wnt signalling regulates nuclear export of Setdb1 during skeletal muscle terminal differentiation. Cell Discovery 2, 16037.

10. Matsui, T., Leung, D., Miyashita, H., Maksakova, I.A., Miyachi, H., Kimura, H., Tachibana, M., Lorincz, M.C., and Shinkai, Y. (2010). Proviral silencing in embryonic stem cells requires the histone methyltransferase ESET. Nature 464, 927–931. 10.1038/nature08858.

11. Murphy, M.M., Lawson, J.A., Mathew, S.J., Hutcheson, D.A., and Kardon, G. (2011). Satellite cells, connective tissue fibroblasts and their interactions are crucial for muscle regeneration. Development 138, 3625–3637. 10.1242/dev.064162.

12. Chakkalakal, J.V., Jones, K.M., Basson, M.A., and Brack, A.S. (2012). The aged niche disrupts muscle stem cell quiescence. Nature 490, 355–360. 10.1038/nature11438.

13. Chang, C.C., Chuang, S.-T., Lee, C.Y., and Wei, J.W. (1972). Role of cardiotoxin and phospholipase A in the blockade of nerve conduction and depolarization of skeletal muscle induced by cobra venom. British Journal of Pharmacology 44, 752–764. 10.1111/j.1476-5381.1972.tb07313.x.

14. Cooper, A.J.L., and Hanigan, M.H. (2018). Metabolism of Glutathione S-Conjugates: Multiple Pathways. In Comprehensive Toxicology (Elsevier), pp. 363–406. 10.1016/B978-0-12-801238-3.01973-5.

15. Ramsay, E.E., and Dilda, P.J. (2014). Glutathione S-conjugates as prodrugs to target drug-resistant tumors. Front. Pharmacol. 5. 10.3389/fphar.2014.00181.

16. Karimi, M.M., Goyal, P., Maksakova, I.A., Bilenky, M., Leung, D., Tang, J.X., Shinkai, Y., Mager, D.L., Jones, S., Hirst, M., et al. (2011). DNA Methylation and SETDB1/H3K9me3 Regulate Predominantly Distinct Sets of Genes, Retroelements, and Chimeric Transcripts in mESCs. Cell Stem Cell 8, 676–687. 10.1016/j.stem.2011.04.004.

17. Zhang, S.-M., Cai, W.L., Liu, X., Thakral, D., Luo, J., Chan, L.H., McGeary, M.K., Song, E., Blenman, K.R.M., Micevic, G., et al. (2021). KDM5B promotes immune evasion by recruiting SETDB1 to silence retroelements. Nature 598, 682–687. 10.1038/s41586-021-03994-2.

18. Griffin, G.K. Epigenetic silencing by SETDB1 suppresses tumour intrinsic immunogenicity. 28.

19. Hopfner, K.-P., and Hornung, V. (2020). Molecular mechanisms and cellular functions of cGAS–STING signalling. Nat Rev Mol Cell Biol 21, 501–521. 10.1038/s41580-020-0244-x.

20. Fajgenbaum, D.C., and June, C.H. (2020). Cytokine Storm. N Engl J Med 383, 2255–2273. 10.1056/NEJMra2026131.

21. Satija, R., Farrell, J.A., Gennert, D., Schier, A.F., and Regev, A. (2015). Spatial reconstruction of single-cell gene expression data. Nat Biotechnol 33, 495–502. 10.1038/nbt.3192.

22. Rosvall, M., and Bergstrom, C.T. (2011). Multilevel Compression of Random Walks on Networks Reveals Hierarchical Organization in Large Integrated Systems. PLoS ONE 6, e18209. 10.1371/journal.pone.0018209.

23. Street, K., Risso, D., Fletcher, R.B., Das, D., Ngai, J., Yosef, N., Purdom, E., and Dudoit, S. (2018). Slingshot: cell lineage and pseudotime inference for single-cell transcriptomics. BMC Genomics 19, 477. 10.1186/s12864-018-4772-0.

24. Galluzzo, C., Chiapparoli, I., Corrado, A., Cantatore, F.P., Salvarani, C., and Pipitone, N. (2023). Rare forms of inflammatory myopathies - part II, localized forms. Expert Review of Clinical Immunology 19, 185–191. 10.1080/1744666X.2023.2154655.

25. Chung, M.-I., Bujnis, M., Barkauskas, C.E., Kobayashi, Y., and Hogan, B.L.M. (2018). Niche-mediated BMP/SMAD signaling regulates lung alveolar stem cell proliferation and differentiation. Development 145, dev163014. 10.1242/dev.163014.

26. Chuong, E.B., Elde, N.C., and Feschotte, C. (2017). Regulatory activities of transposable elements: from conflicts to benefits. Nat Rev Genet 18, 71–86. 10.1038/nrg.2016.139.

27. De Cecco, M., Criscione, S.W., Peterson, A.L., Neretti, N., Sedivy, J.M., and Kreiling, J.A. (2013). Transposable elements become active and mobile in the genomes of aging mammalian somatic tissues. Aging 5, 867–883. 10.18632/aging.100621.

28. Valdebenito-Maturana, B., Valdebenito-Maturana, F., Carrasco, M., Tapia, J.C., and Maureira, A. (2022). Activation of Transposable Elements in Human Skeletal Muscle Fibers upon Statin Treatment. IJMS 24, 244. 10.3390/ijms24010244.

29. Schoggins, J.W., Wilson, S.J., Panis, M., Murphy, M.Y., Jones, C.T., Bieniasz, P., and Rice, C.M. (2011). A diverse range of gene products are effectors of the type I interferon antiviral response. Nature 472, 481–485. 10.1038/nature09907.

30. Haag, S.M., Gulen, M.F., Reymond, L., Gibelin, A., Abrami, L., Decout, A., Heymann, M., van der Goot, F.G., Turcatti, G., Behrendt, R., et al. (2018). Targeting STING with covalent small-molecule inhibitors. Nature 559, 269–273. 10.1038/s41586-018-0287-8.

31. de Oliveira Mann, C.C., Orzalli, M.H., King, D.S., Kagan, J.C., Lee, A.S.Y., and Kranzusch, P.J. (2019). Modular Architecture of the STING C-Terminal Tail Allows Interferon and NF-κB Signaling Adaptation. Cell Reports 27, 1165-1175.e5. 10.1016/j.celrep.2019.03.098.

32. Glück, S., Guey, B., Gulen, M.F., Wolter, K., Kang, T.-W., Schmacke, N.A., Bridgeman, A., Rehwinkel, J., Zender, L., and Ablasser, A. (2017). Innate immune sensing of cytosolic chromatin fragments through cGAS promotes senescence. Nat Cell Biol 19, 1061–1070. 10.1038/ncb3586.

33. Gulen, M.F., Koch, U., Haag, S.M., Schuler, F., Apetoh, L., Villunger, A., Radtke, F., and Ablasser, A. (2017). Signalling strength determines proapoptotic functions of STING. Nat Commun 8, 427. 10.1038/s41467-017-00573-w.

34. Zierhut, C., Yamaguchi, N., Paredes, M., Luo, J.-D., Carroll, T., and Funabiki, H. (2019). The Cytoplasmic DNA Sensor cGAS Promotes Mitotic Cell Death. Cell 178, 302-315.e23. 10.1016/j.cell.2019.05.035.

35. Hadjadj, J., Yatim, N., Barnabei, L., Corneau, A., Boussier, J., Smith, N., Péré, H., Charbit, B., Bondet, V., Chenevier-Gobeaux, C., et al. (2020). Impaired type I interferon activity and inflammatory responses in severe COVID-19 patients. Science 369, 718–724. 10.1126/science.abc6027.

36. Tovo, P.-A., Garazzino, S., Daprà, V., Pruccoli, G., Calvi, C., Mignone, F., Alliaudi, C., Denina, M., Scolfaro, C., Zoppo, M., et al. (2021). COVID-19 in

Children: Expressions of Type I/II/III Interferons, TRIM28, SETDB1, and Endogenous Retroviruses in Mild and Severe Cases. IJMS 22, 7481. 10.3390/ijms22147481.

37. Perez-Valera, M., Martinez-Canton, M., Gallego-Selles, A., Galván-Alvarez, V., Gelabert-Rebato, M., Morales-Alamo, D., Santana, A., Martin-Rodriguez, S., Ponce-Gonzalez, J.G., Larsen, S., et al. (2021). Angiotensin-Converting Enzyme 2 (SARS-CoV-2 receptor) expression in human skeletal muscle. Scand J Med Sci Sports 31, 2249–2258. 10.1111/sms.14061.

38. Shi, Z., de Vries, H.J., Vlaar, A.P.J., van der Hoeven, J., Boon, R.A., Heunks, L.M.A., and Ottenheijm, C.A.C. (2021). Diaphragm Pathology in Critically Ill Patients With COVID-19 and Postmortem Findings From 3 Medical Centers. JAMA Intern Med 181, 122–124. 10.1001/jamainternmed.2020.6278.

39. Mittal, A., Dua, A., Gupta, S., and Injeti, E. (2021). A research update: Significance of cytokine storm and diaphragm in COVID-19. Current Research in Pharmacology and Drug Discovery 2, 100031. 10.1016/j.crphar.2021.100031.

40. Theret, M., Mounier, R., and Rossi, F. (2019). The origins and non-canonical functions of macrophages in development and regeneration. Development 146, dev156000. 10.1242/dev.156000.

41. Bao, T., Liu, J., Leng, J., and Cai, L. (2021). The cGAS–STING pathway: more than fighting against viruses and cancer. Cell Biosci 11, 209. 10.1186/s13578-021-00724-z.

42. Ou, L., Zhang, A., Cheng, Y., and Chen, Y. (2021). The cGAS-STING Pathway: A Promising Immunotherapy Target. Front. Immunol. 12, 795048. 10.3389/fimmu.2021.795048.

43. Wang, Q., Bergholz, J.S., Ding, L., Lin, Z., Kabraji, S.K., Hughes, M.E., He, X., Xie, S., Jiang, T., Wang, W., et al. (2022). STING agonism reprograms tumor-associated macrophages and overcomes resistance to PARP inhibition in BRCA1-deficient models of breast cancer. Nat Commun 13, 3022. 10.1038/s41467-022-30568-1.

44. Miao, L., Qi, J., Zhao, Q., Wu, Q.-N., Wei, D.-L., Wei, X.-L., Liu, J., Chen, J., Zeng, Z.-L., Ju, H.-Q., et al. (2020). Targeting the STING pathway in tumor-associated macrophages regulates innate immune sensing of gastric cancer cells. Theranostics 10, 498–515. 10.7150/thno.37745.

45. Qian, B.-Z., and Pollard, J.W. (2010). Macrophage Diversity Enhances Tumor Progression and Metastasis. Cell 141, 39–51. 10.1016/j.cell.2010.03.014.

46. Bassez, G., Authier, F.-J., Lechapt-Zalcman, E., Delfau-Larue, M.H., Plonquet, A., Coquet, M., Illa, I., and Gherardi, R.K. (2003). Inflammatory Myopathy with Abundant Macrophages (IMAM): A Condition Sharing Similarities with Cytophagic Histiocytic Panniculitis and Distinct from Macrophagic Myofasciitis. J Neuropathol Exp Neurol 62, 464–474. 10.1093/jnen/62.5.464.

47. Brunn, A., Hans, V.J., Vogelgesang, S., and Deckert, M. (2009). Inflammatory myopathy with abundant macrophages and dermatomyositis: two stages of one disorder or two distinct entities? Acta Neuropathol 118, 793–801. 10.1007/s00401-009-0570-8.

48. Zhou, M., Cheng, X., Zhu, W., Jiang, J., Zhu, S., Wu, X., Liu, M., and Fang, Q. (2022). Activation of cGAS-STING pathway – A possible cause of myofiber atrophy/necrosis in dermatomyositis and immune-mediated necrotizing myopathy. Journal of Clinical Laboratory Analysis 36, e24631. 10.1002/jcla.24631.

49. Zhang, R.-H., Judson, R.N., Liu, D.Y., Kast, J., and Rossi, F.M.V. (2016). The lysine methyltransferase Ehmt2/G9a is dispensable for skeletal muscle development and regeneration. Skeletal Muscle 6, 22. 10.1186/s13395-016-0093-7.

50. Biferali, B., Bianconi, V., Perez, D.F., Kronawitter, S.P., Marullo, F., Maggio, R., Santini, T., Polverino, F., Biagioni, S., Summa, V., et al. (2021). Prdm16-mediated H3K9 methylation controls fibro-adipogenic progenitors identity during skeletal muscle repair. Sci. Adv. 7, eabd9371. 10.1126/sciadv.abd9371.

51. Bulut-Karslioglu, A., De La Rosa-Velázquez, I.A., Ramirez, F., Barenboim, M., Onishi-Seebacher, M., Arand, J., Galán, C., Winter, G.E., Engist, B., Gerle, B., et al. (2014). Suv39h-Dependent H3K9me3 Marks Intact Retrotransposons and Silences LINE Elements in Mouse Embryonic Stem Cells. Molecular Cell 55, 277–290. 10.1016/j.molcel.2014.05.029.

52. Brun, C.E., Wang, Y.X., and Rudnicki, M.A. (2018). Single EDL Myofiber Isolation for Analyses of Quiescent and Activated Muscle Stem Cells. In Cellular Quiescence Methods in Molecular Biology., H. D. Lacorazza, ed. (Springer New York), pp. 149–159. 10.1007/978-1-4939-7371-2_11.

53. Meier, F., Brunner, A.-D., Koch, S., Koch, H., Lubeck, M., Krause, M., Goedecke, N., Decker, J., Kosinski, T., Park, M.A., et al. (2018). Online Parallel Accumulation–Serial Fragmentation (PASEF) with a Novel Trapped Ion Mobility Mass Spectrometer. Molecular & Cellular Proteomics 17, 2534–2545. 10.1074/mcp.TIR118.000900.

54. Zeng, W., Yue, L., Lam, K.S.W., Zhang, W., So, W.-K., Tse, E.H.Y., and Cheung, T.H. (2022). CPEB1 directs muscle stem cell activation by reprogramming the translational landscape. Nat Commun 13, 947. 10.1038/s41467-022-28612-1.

55. Zhu, W., Smith, J.W., and Huang, C.-M. (2010). Mass Spectrometry-Based Label-Free Quantitative Proteomics. Journal of Biomedicine and Biotechnology 2010, 1–6. 10.1155/2010/840518.

Supplementary Figures

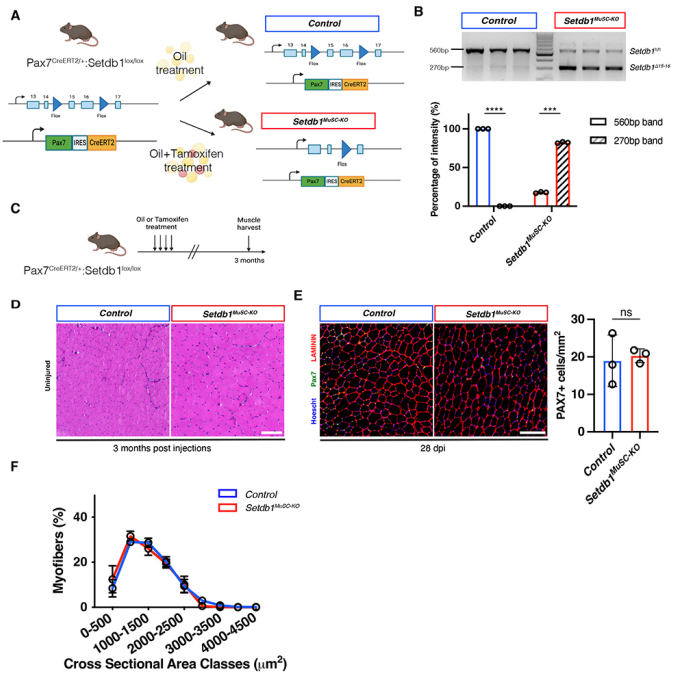

Figure S1, related to figure 1. The loss of Setdb1 does not affect muscle homeostasis. *(A) Conditional knock-out of Setdb1 in adult MuSCs using Tamoxifen-inducible CRE under the MuSC specific PAX7 promoter. (B) Genotyping of Control and Setdb1$^{MuSC\text{-}KO}$ cells in vitro and quantification of the band intensity (n=3 mice). (C) Experimental scheme; Pax7$^{CRE\text{-}ERT2}$; Setdb1$^{fl/fl}$ mice intraperitoneally injected with either Oil or Tamoxifen and are harvested 3 months after the injections. (D) Quantification of PAX7+ cells in Setdb1$^{+/+}$ and Control and Setdb1$^{MuSC\text{-}KO}$ muscles in vivo (n=3 mice). (E) Hematoxylin and eosin stain of TA (Tibialis Anterior) muscle cross sections at 3 months after oil and tamoxifen injections (n=3 mice). (F) Distribution of cross sectional area of TA muscles of Control and Setdb1$^{MuSC\text{-}KO}$ TA muscles at 3 months after injections. Data are represented as mean ± SEM; n.s not significant, $^{***}p < 0.001$, t test. Scale bar, (D) 50 µm, (E) 50 µm.*

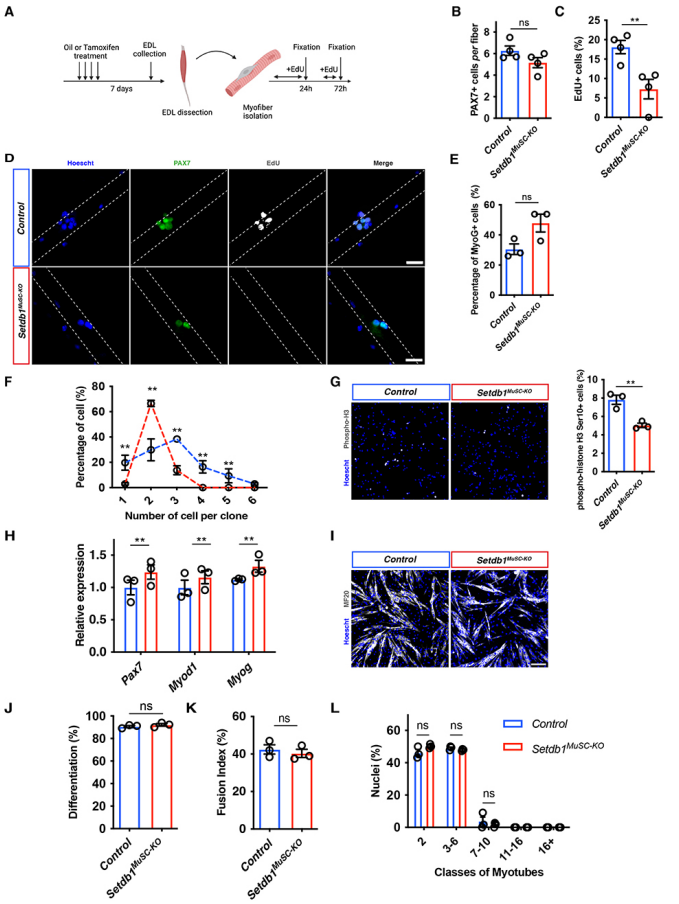

Figure S2 related to figure 2. The loss of Setdb1 promotes cell cycle defect but does not impact muscle differentiation in vitro. *(A) Experimental set up of isolated myofibers ex vivo during 24 and 72 hours after oil and Tamoxifen treatment in the Pax7$^{CRE\text{-}ERT2}$; Setdb1$^{fl/fl}$ mice. (B) Immunostaining against PAX7 and EdU at 72 hours after myofiber isolation ex vivo. (C) Quantification of PAX7+ cells on isolated myofiber after 24h in culture ex vivo in Control and Setdb1$^{MuSC\text{-}KO}$ conditions (n=4). (D) Quantification of EdU+ cells on isolated myofiber after 24 hours in culture ex vivo in Control and Setdb1$^{MuSC\text{-}KO}$ cells (n=4). (E) Quantification of MYOG+ cells on isolated myofiber after 72h in culture ex vivo in Control and Setdb1$^{MuSC\text{-}KO}$ cells (n=3). (F) Clonal assay showing the number of cell per clone after 8 days in Control and Setdb1$^{MuSC\text{-}KO}$ condition (n=3). (G) Immunostaining against phospho-Histone 3 in vitro after 5 days of ethanol or 4-hydroxitamoxifen treatment and quantification of the phospho-histone H3+ cells (n=3). (H) Relative expression of Pax7, Myod1 and Myog in MuSCs in vitro after 5 days of ethanol or 4-hydroxitamoxifen treatment (n=3). (I) Immunostaining against MF20 in Control and Setdb1$^{MuSC\text{-}KO}$ cells in vitro after 3 days of differentiation (n=3). (J) Quantification of the percentage of fused cells in Control and Setdb1$^{MuSC\text{-}KO}$ conditions (n=3). (K) Quantification of the percentage of differentiated cells in Control and Setdb1$^{MuSC\text{-}KO}$ conditions (n=3). (L) Proportion of the number of nuclei in the Control and Setdb1$^{MuSC\text{-}KO}$ conditions in vitro (n=3). Data are represented as mean ± SEM; n.s not significant, $^{**}p < 0.01$, t test.*

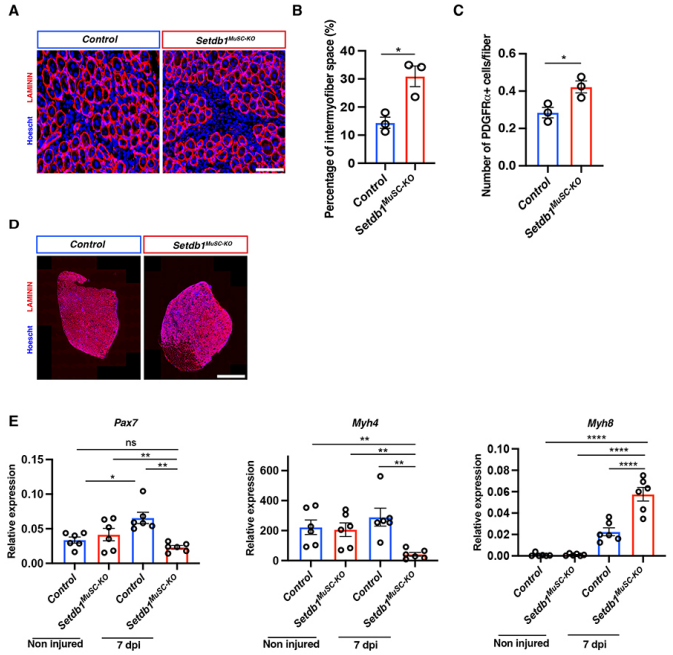

Figure S3, related to figure 3. The muscle regeneration process is affected by the loss of Setdb1 at 4dpi and 7dpi. *(A) Immunostaining against LAMININ in TA (Tibialis Anterior) muscle cross sections after cardiotoxin (CTX) injection at 4 days after injury in Control and Setdb1$^{MuSC\text{-}KO}$ conditions (n=3 mice). (B) Quantification of the intermyofiber space in the Control and Setdb1$^{MuSC\text{-}KO}$ conditions. (C) Immunostaining against PDGFRα in TA muscle cross sections after CTX injection at 4 days after injury in Control and Setdb1$^{MuSC\text{-}KO}$ muscles and quantification of the number of PDGFRα+ cells (n=3 mice). (D) Immunostaining against LAMININ in TA muscle cross sections after CTX injection at 7 days after injury in Control and Setdb1$^{MuSC\text{-}KO}$ muscles (n=3). (E) RT-qPCR of Pax7, Myh4 and Myh8 on TA cryosections at uninjured or 7 days after CTX in Control and Setdb1$^{MuSC\text{-}KO}$ muscles (n=6). Data are represented as mean ± SEM; n.s not significant, $^{*}p < 0.05$, $^{**}p < 0.01$, $^{****}p < 0.0001$.Scale bars, (A) 50 µm, (D) 200 µm.*

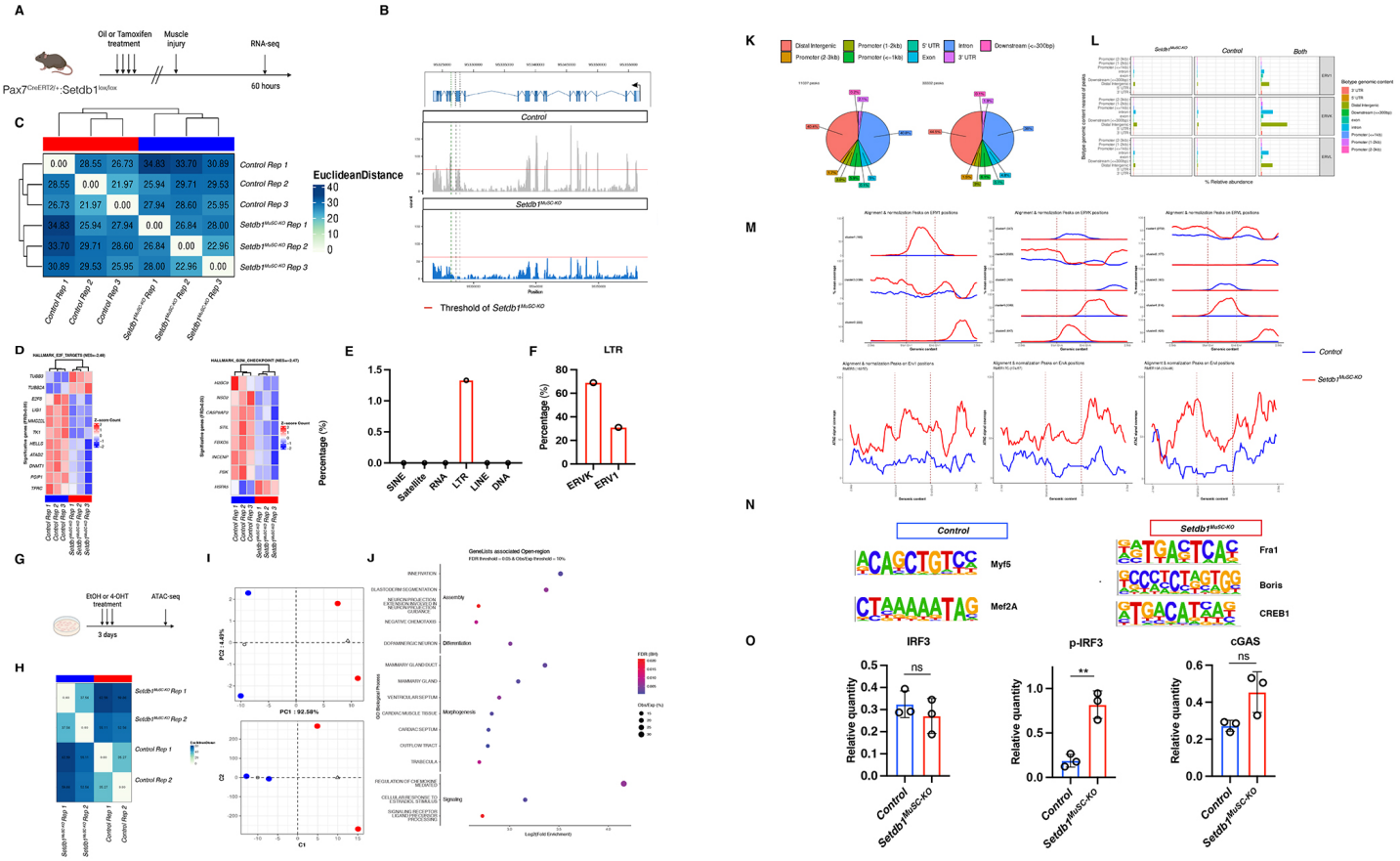

Figure S4, related to figure 4. The loss of Setdb1 promotes ERV de-repression and inflammation. Part 1. *(A) Experimental set up; Pax7$^{CRE-ERT2}$; Setdb1$^{fl/fl}$ mice intraperitoneally injected with either Oil or Tamoxifen and RNA-seq was performed on sorted MuSCs 60 hours after CTX injury on TA (Tibialis Anterior) muscle. (B). Unsupervised clustering of the RNA-seq samples over similarities and dissimilarities by sample from Euclidean distance matrix on the 1000 most variable expression genes. (C) Tracks of reads mapped on Setdb1 gene (ENSMUSG00000015697) superposed on canonical transcript (ENSMUST00000015841,12).in the Control and Setdb1$^{MuSC-KO}$ cells. (D) Heatmap of RNA-seq normalized expression z-scores computed on significative genes (FDR < 0.05) for hallmark E2F target and G2M checkpoint in the Control and Setdb1$^{MuSC-KO}$ cells (n=3 mice). Genes and samples are clustered using euclidean matrix. (E) Percentage of the different transposable element families found in the Control and Setdb1$^{MuSC-KO}$ cells. (F) Percentage of the different Long Terminal Repeat found in the Control and Setdb1$^{MuSC-KO}$ cells. (G) Experimental set up; Pax7$^{CRE-ERT2}$; Setdb1$^{fl/fl}$ MuSCs were treated with either ethanol or 4-hydroxitamoxifen during 3 days and ATAC-seq was performed. (H) Visualizing the overall effect of experimental covariates and batch effects using first (PC1) and second (PC2) Principal Component Analysis (PCA) dimension (in top) and first (C1) and second (C2) Uniform Manifold Approximation and Projection (UMAP) dimensions (in bottom) on the 1000 most variable expression peaks. (I) Unsupervised clustering of the ATAC-seq samples over similarities and dissimilarities by sample from euclidean distance matrix on the 1000 most variable expression genes.(J) Functional enrichment analysis directly performed on genomic regions by rGREAT tool on open-region between Control and Setdb1$^{MuSC-KO}$ (n=2). Dot in red indicate a high significant enrichment (adjusted by FDR), dot in blue indicate a low significant enrichment. The size shows the number of open-region associated to gene in process (observation) on the number of open-region associated to all gene in the same process (expected). Results are ordering in high to low level of Log2 Fold Change. Selected enriched terms are presented according to the significativity of results (FDR < 0,05) and ratio observation/expected >= 10%.. (K) Pie plot representing the different type of genomic regions opened in the Control and Setdb1$^{MuSC-KO}$ cells. (L) Relative abundance of the different locations of the ERV found in the Control and Setdb1$^{MuSC-KO}$ cells inside each genomic regions opened. (M) Footprinting K-mean and ATAC signal coverage of the different ERV families found in the Control and Setdb1$^{MuSC-KO}$ cells. (N) Position Weight Matrix (PWM) using Hypergeometric Optimization of Motif EnRichment (Homer) found in the Control and Setdb1$^{MuSC-KO}$ cells based on known references motifs. (O) Western blot quantification of IRF3, p-IRF3 and cGAS in Control and Setdb1$^{MuSC-KO}$ cells in vitro (n=3). Data are represented as mean ± SEM; n.s not significant, $^{**}p < 0.01$, t test.*

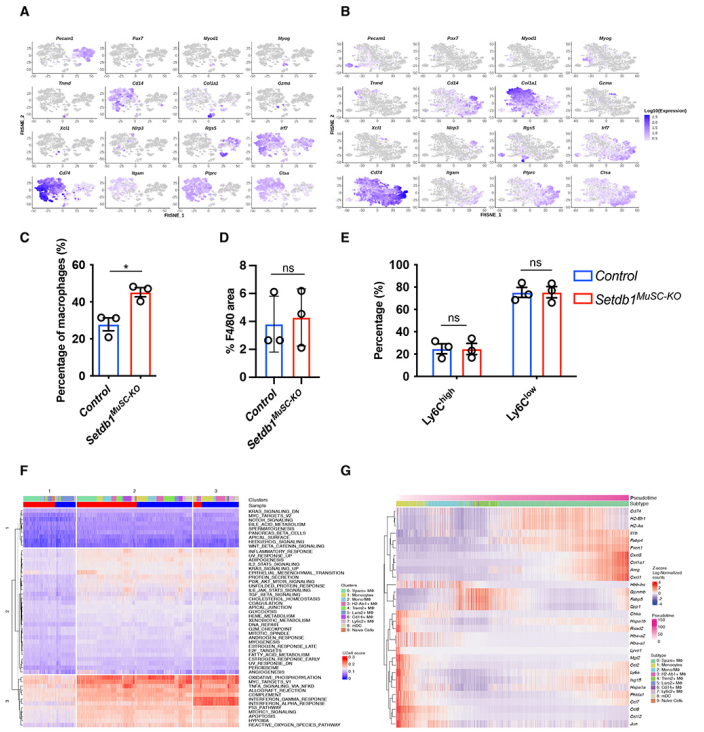

Figure S5, related to figure 5. Single cell RNA-seq analysis demonstrating that the loss of Setdb1 leads to an inflammatory phenotype. *(A) Feature Plot projected on a FltSNE dimensional reduction of the scRNA-seq from the Control condition. Each graph shows the expression pattern of a selected canonical marker used to identify the different populations. Cells are color-coded according to the intensity of the marker shown. (B) Feature Plot projected on a FltSNE dimensional reduction of the scRNA-seq from the Setdb1$^{MuSC\text{-}KO}$ condition. Each graph shows the expression pattern of a selected canonical marker used to identify the different populations. Cells are color-coded according to the intensity of the marker shown. (C) Percentage of macrophages found in Control and Setdb1$^{MuSC\text{-}KO}$ mice using flow cytometry at 4 days after TA (Tibialis Anterior) injury using cardiotoxin (CTX) (n=3 mice). (D. Quantification of the F4/80 area found in the Control and Setdb1$^{MuSC\text{-}KO}$ mice at 4 days after TA CTX injury (n=3 mice). (E) Percentage of pro and anti-inflammatory macrophages found in Control and Setdb1$^{MuSC\text{-}KO}$ mice using flow cytometry at 4 days after TA injury using CTX (n=3). (F) Heatmap of Mouse Hallmark from MSigDB by UCell score based on the relative ranking of genes for individual cells. K-means clustering was performed in 3 different levels of enrichment: low, middle and high. Columns were reorder by clusters and samples. (G) Heatmap of top100 high variables genes differentially expressed along the fourth calculated trajectory of Setdb1$^{MuSC\text{-}KO}$ condition. Data are represented as mean ± SEM; n.s not significant, $^{*}p < 0.05$, t test.*

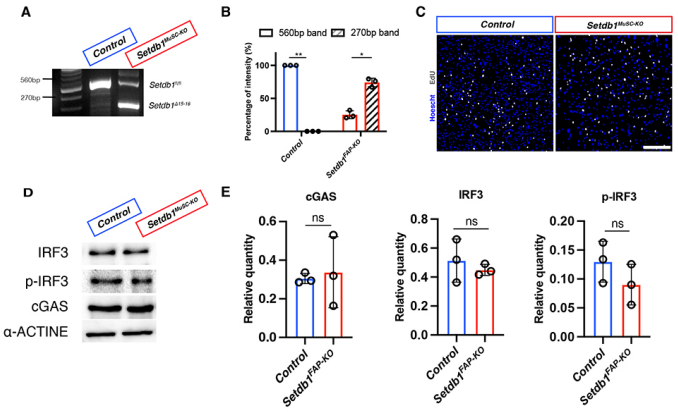

Figure S6, related to figure 7. The loss of Setdb1 in FAPs does not lead to any phenotype in vitro. *(A) Genotyping of Control and Setdb1$^{FAP\text{-}KO}$ fibroblasts in vitro and quantification of the band intensity. (B) Quantification of the band intensity of Control and Setdb1$^{FAP\text{-}KO}$ fibroblasts in vitro. (C) Immunostaining against EdU in Control and Setdb1$^{FAP\text{-}KO}$ fibroblasts in vitro and quantification of EdU+ cells in both conditions. (D) Western blot analysis of IRF3 (55 kDa), p-IRF3 (55 kDa) and cGas (60 kDa) in Control and Setdb1$^{FAP\text{-}KO}$ fibroblasts in vitro and quantification of the relative quantity. (E) Western blot quantification of IRF3, p-IRF3 and cGas in Control and Setdb1$^{FAP\text{-}KO}$ fibroblasts in vitro and quantification of the relative quantity. Data are represented as mean ± SEM; n.s not significant, $^{*}p < 0.05$, $^{**}p < 0.01$, t test. Scale bar, (C) 150 µm.*